TUHH ims
Institute of
Multiphase Flows

Master Thesis

Design, Construction and Evaluation of Lagrangian Sensor Particles for the Flow Behavior Determination in a 200 L and 15000 L Bioreactor

By Paramveer Singh GopalSingh

First Examiner: Prof. Dr.-Ing. Michael Schlüter
Second Examiner: Prof. Dr.-Ing. Hoc Khiem Trieu
Supervisor: Sebastian Hofmann, M.Sc.

01.01.2023 - 30.06.2023

Eidesstattliche Erklärung

Hiermit versichere ich, dass ich die vorliegende Arbeit selbstständig verfasst und keine anderen als die angegebenen Quellen und Hilfsmittel benutzt habe, dass alle Ausführungen, die anderen Schriften wörtlich oder sinngemäß entnommen wurden, kenntlich gemacht sind und dass die Arbeit in gleicher oder ähnlicher Fassung noch nicht Bestandteil einer Studien- oder Prüfungsleistung war.

Hamburg, den _____ Unterschrift: _____

Contents

List of Tables

List of Symbols, Units and Abbreviations

Symbols

Symbol	Significance	Units
d_1	Reactor diameter	m
d_2	Impeller Diameter	m
d_P	Particle Diameter	m
v_{tip}	Impeller Tip Velocity	$^{-1}$
$\bar{v_{tip}}$	Average Impeller Tip Velocity	$^{-1}$
ϵ_θ	Energy Dissipation Rate	W kg^{-1}
P	Power supplied from the stirrer	W
V	Volume of the reactor	m^3
ρ_f	Density of fluid	kg m^{-3}
n	Rotation Frequency of the Impeller	s^{-1}
Ne	Newton number	-
ω_o^t	Translational Angular Velocity	$^\circ$ s^{-1}
a_o^t	Translational Acceleration	m s^{-2}
ρ_{app}	Apparent Density of Reactor Fluid	kg m^{-3}
ρ_l	Liquid density	kg m^{-3}
ρ_g	Gas density	kg m^{-3}
ρ_P	Particle Density	kg m^{-3}
ϵ	Volumetric Gas Holdup	-
H_L	Height of the Liquid in Reactor	m
W_d	Baffle width	m
R_{d2d1}	Impeller diameter to Reactor Diameter ratio	
z/H_L	Normalized Height	-

a_{mag}	acceleration magnitude	m s^{-2}
v_{mag}	Velocity magnitude	m s^{-1}
g	Acceleration due to Gravity	m s^{-2}
$a_x(t)$	acceleration in X axis as a function of time	m s^{-2}
ϕ	Roll - Angular movement around X axis	°
θ	Pitch - Angular movement around Y axis	°
ψ	Yaw - Angular movement around Z axis	°
ρ_f	Density of fluid phase	kg m^{-3}
$\rho_{solution}$	Density of the sodium chloride solution	kg m^{-3}
$c_{mass,NaCl}$	Mass concentration of sodium chloride	kg kg^{-1}

Abbreviations

Abbr.	Definition
Computer Numerical Control	CNC
CHO	Chinese Hamster Ovary
CFD	Computational Fluid Dynamics
IP	Instrumented Particle
CTV	Capsule Tracking Velocimetry
PTV	Particle Tracking Velocimetry
RD	Rushton Disk turbine
PB	Pitched Blade turbine
PU	Pressure Unit
RTPB	Ruston Turbine Pitch Blade
PBPB	Pitch Blade Pitch Blade
PBPBPB	Pitch Blade Pitch Blade Pitch Blade
MEMS	Micro Electro Mechanical System
DOF	Degrees of Freedom
ESKF	Error State Kalman Filter
I2C/ I^2C	Inter-Integrated Circuit
LED	Light Emitting Diode
FAT	File Allocation Table
IMU	Inertial Measurement Unit
LSP	Lagrangian Sensor Particle

PMMA	Poly(methyl methacrylate)
STR	Stirred Tank Reactor
PDF	Probability Distribution Function

Abstract

Stirred Tank Reactors (STRs) are frequently employed in the bioprocessing industry to produce bioproducts employing bacterial, yeast, or mammalian cell lines. The productivity of these reactors may be impacted when they grow in size due to the presence of heterogeneous zones. Using the Lagrangian measurement approach with free-flowing sensors is one way to look at these heterogeneities. In this thesis, two Lagrangian Sensor Particles (LSPs) that can be made using off-the-shelf components and a shell that can be produced by computer numerical control (CNC) machining are designed and built to circumvent this problem and study the heterogeneities in STRs. One type of LSP was built around an Inertial Measurement Unit (IMU), and the second was built around a pressure sensor. They are built to have a density between 1000 and 1005 kgm^{-3}.

These LSPs are then tested in a 200 L and 15000 L reactor. Particle Tracking Velocimetry (PTV) is performed on the LSP in the 200 L reactor. The distribution of acceleration, velocity, and axial position is then determined using the LSPs. The data obtained via Particle Tracking Velocimetry (PTV) is then compared with the data obtained from the LSPs. A steady increase in axial velocity is seen with increasing impeller speeds, according to data from pressure and IMU sensors.

Thus, a modular Lagrangian Sensor Particle (LSP) is developed, which can help investigate heterogeneities in STRs by making the LSP platform widely accessible, providing consistent results for all types of sensors. Enhancing the sensor module, the microcontroller, and the data processing method can further expand these findings.

Zusammenfassung

Stirred Tank Reactors (STRs) werden häufig in der biotechnologischen Industrie eingesetzt, um biologische Produkten unter Verwendung von Bakterien-, Hefe- oder Säugetierzelllinien herzustellen. Die Produktivität dieser Reaktoren kann mit zunehmender Größe durch das Vorhandensein heterogener Zonen beeinträchtigt werden. Die Verwendung des Lagrangeschen Messansatzes mit frei fließenden Sensoren ist eine Möglichkeit, diese Heterogenitäten zu untersuchen. In dieser Arbeit werden zwei Typen Lagrangescher Sensorpartikel (LSP), die aus handelsüblichen Komponenten in einer CNC-gefertigten Schale zusammengesetzt werden können, entwickelt und gebaut, die Heterogenitäten in STRs zu untersuchen. Ein Typ von LSP wurde um eine Inertial Measurement Unit (IMU) herum gebaut, der zweite um einen Drucksensor herum. Sie wurden so gebaut, dass sie eine Dichte zwischen 1000 und 1005 $\mathrm{kgm}^{-3} haben$.

Diese LSPs werden dann in einem 200-Liter- und einem 15000-Liter-Reaktor getestet. Die Particle Tracking Velocimetry (PTV) wird an den LSP im 200-Liter-Reaktor durchgeführt. Anschließend wird die Verteilung von Beschleunigung, Geschwindigkeit und axialer Position der LSP bestimmt. Die mit der Particle Tracking Velocimetry (PTV) gewonnenen Daten werden dann mit den aus den LSP gewonnenen Daten verglichen. Die Daten der Druck- und IMU-Sensoren zeigen, dass die Axialgeschwindigkeit mit zunehmender Drehzahl des Rührers stetig ansteigt.

Auf diese Weise wird ein modulares Lagrangesches Sensorteilchen (LSP) entwickelt, das zur Untersuchung von Heterogenitäten in STRs beitragen kann, indem es die LSP-Plattform allgemein zugänglich macht und konsistente Ergebnisse für alle Arten von Sensoren liefert. Durch die Verbesserung des Sensormoduls, des Mikrocontrollers und

der Datenverarbeitungsmethode können diese Erkenntnisse weiter ausgebaut werden.

1. Introduction and Motivation

The use of large-scale bioreactors has become increasingly popular in the bioprocess industry. These bioreactors are utilized for the production of crucial products, ranging from fermentation products derived from primary or secondary metabolites from bacterial or fungal cultures to high-value products from mammalian cell cultures. These products can be used in various ways, such as nutritional supplements like vitamins or as production aids for food products like enzymes. The products obtained from biotechnology are also used in very niche areas like the medical field, like for the production of antibiotics or vaccines. Most bio-pharmaceutical products are produced using the Chinese Hamster Ovary (CHO) cell line. The CHO cells are used to produce a number of important bio-pharmaceuticals like monoclonal antibodies, vaccines, and other proteins. This is because of the ability of CHO cells to phosphorylate the respective products to be used for consumption by humans and other mammals.[Agg14, Jad13, Hac09, Ahm22]

The use of CHO cell lines for bio-pharmaceutical production is rapidly increasing. With this increase in demand, the need to optimise the production process for cost reduction, quality improvement, and maintenance of product quality is also increasing. The major steps to achieving this include the selection and characterization of the cell line, the selection and optimization of the conditions in which the various production phase take place, the composition of the culture media, and the selection of the bioreactor in which the cell line grows [Kum07, Agg14, Kun16]. The typical size of these bioreactors is around 2 L to 4000 L in volume, with ports open to

insert sensor probes [Tis10, Ros18]. One major challenge for the production comes from the selection and scaling of the production from a small lab-scale reactor to industrial stirred tank reactors. The capacity of these reactors can be as large as 20 m^3 [Sie11]. There are also Single-use bioreactors available for mammalian cell cultures [Jun18]. During scaling, the varied fluid and hydrodynamic interactions in larger bioreactors bring new challenges to bio-product production using STR. There are regions of local heterogeneities in industrial STRs which persist in them even after the amount of effort spent in the scale-up process. These local heterogeneities and compartmentalization can lead to cells staying suspended in the STR by causing a discrepancy in the mixing times [Ros18].

These heterogeneous regions and compartmentalization phenomena may lead to the accumulation of cells in the apoptotic, necrotic, or autophagic phase, which can lead to decreased cell viability and productivity and introduce or increase variability in the final product. This phenomenon is called Quorum sensing, which allows cells to communicate and coordinate their behaviour through the small signalling molecules called autoinducers. They have been shown to have a role in regulating cell death and other behaviours like cell division and gene expression in some industrially used cell lines, which are used in the large-scale production of biopharmaceuticals. Thus the accumulation of cells in these local heterogeneous zones can cause negative effects from the quorum sensing and thus cause issues in production strains [Shr06, Cho07].

Therefore the study of the spatiotemporal distribution of mixing parameters and shear parameters in these bioreactors would help in the optimization and scale-up/scale-down of these reactors [Viv21, Bis21]. As mixing parameters determine the growth and life-cycle of the cells in the bioreactors and the shear forces along with several other factors like pH, nutrient, and dissolved O_2 determine the cell longevity and productivity [Chi09, Bar12]. However, the measurement of these parameters is limited by the sensors that can collect and transmit the data from the reactors. In general, the position of these sensors is limited to the reactor walls as they are

fixed from the ports in the reactor walls. This is especially prominent in large-scale vessels with vessel diameters sufficiently large enough to have areas of blind spots that the sensors are unable to detect. These probes follow the Eulerian 1D approach for measurement, where the point of measurement is fixed, and the fluid moves around or through the respective sensor point [Tro07a]. Therefore, quantising the true process conditions within the bioreactor is difficult due to the fact that only a single or a few fixed points of measurement are available in the reactor, which makes the study of heterogeneities and compartmentalization difficult. [Ros18].

The inhomogeneities are being studied by various methods, including simulation methods like Computational Fluid Dynamics (CFD) and glass or acrylic glass STR with experimental methods using tracers [Pau20, Sie11]. These studies, however, are inherently flawed because it is difficult to reproduce real-world data or gather enough data points because of the limitations of the available sensors. The latter issue is being tackled by various groups working on the mobile sensors, which can move in the reactor fluid while transmitting or recording data from inside the reactor; these sensors are called Lagrangian Sensor Particles (LSP). These LSPs follow the Lagrangian method of data measurement, which involves the determination of the flow properties of the fluid, like velocity, acceleration, etc. At the same time, they are being tracked as they move through a fluid field [Lau19a, Rei17, Bun19, Dui19, Val19, Bun20].

These LSPs have a drawback, which is that they cannot be tracked accurately inside a reactor. Several attempts have been made to address this, for example, with the use of an Inertial Measurement Unit (IMU), use of cameras to enable visual tracking, mapping of magnetic inductions, using a pressure sensor to track the axial position or with a combination of these methods, [Lau17, Thi10, Zim13a, Mro16]. The distribution of particles similar to LSPs has also been tried to be simulated, but these simulations lack experimental verification [Lau19a].

Objective

Many of the sensors used by research groups are propriety material, and the hardware for the same is custom-made, making them very difficult to obtain for experiments [Rei15, Bis20]. Also, tracking these particles is difficult as a significant number of them do not have any location or velocity measuring instruments. This has the problem of estimating the parameters in the reactor from a temporal perspective; however, the spatial perspective is either lacking or inadequate.

This has been tackled in multiple ways, including the utilization of an IMU, positioning instruments like a Global Positioning System (GPS), Potentiometric sensors, etc., or the use of pressure sensors to determine the axial position of the instrument in the reactor vessel [Bis20, Bis21, Lau19a].

This work aims to design and construct Instrumented Lagrangian Sensor Particles (LSPs) and subsequently apply them in the study of flow behaviour in industrial-sized bioreactors by resolving the spatiotemporal data.

The first objective of this body of work is to design, construct, and program LSPs using commercially available instruments, including sensors, micro-controllers, etc., and a shell that can be made from Poly(methyl methacrylate) (PMMA) using a Computer Numerical Control (CNC) machine. The second objective is to test the LSPs and to obtain an analysis of the acceleration, velocity, and position distribution data, hereon referred to as internal data, against data obtained by visual methods (Camera setup), referred to as external data. This was done by testing them in 200L and 15000L working volumes bioreactors. This study is a part of the Priority Program SPP 2170 "InterZell" (funded by the German Research Foundation - Deutsche Forschungsgemeinschaft).

2. Theoretical Principles and State-of-the-Art

This chapter covers the theoretical basis and state of the art. The first part of this chapter describes bioreactors, how they behave, and the state of the art of their sensors. The second part of the chapter discusses the various Lagrangian Sensor Particles in development and how tracking the same works in the volume of the reactor. The third part of the chapter briefly talks about a study of axial tracking of mobile sensor particles in reactors. The last part of this chapter summarizes the tracking of particles using pressure sensors and Inertial Measurement Units(IMU).

2.1. Bioreactors

As stated by Martin et al. [Mar04], bioreactors are defined as "devices in which biological and/or biochemical processes develop under closely monitored and tightly controlled environmental and operating conditions (e.g., pH, temperature, pressure, nutrient supply, waste removal etc.,)". They are available in various sizes and used in various industries like food industries for producing products like synthetic vitamins or in pharmaceutical industries for producing high-value products like recombinant proteins and antibodies or processes like industrial wastewater treatment [Mar05]. The main purpose of a bioreactor is to provide a suitable environment for the cells or enzymes to transform substrates to desired products, which is done by careful control of factors like substrate concentration, dissolved oxygen and carbon dioxide levels, and pH, to state a few examples.

These variables must be controlled very closely as any change to them can adversely affect the cells and thereby affect the yield of the product [Moo11].

There are several ways to classify bioreactors, such as by their mode of operation, which includes batch, fed-batch, or continuous, or by the type of electron acceptor, such as aerobic, anaerobic, or micro-aerobic conditions. They can also be categorized based on the method of agitation, including mechanically agitated tanks, air-lift columns, bubble columns, or membrane reactors. Another way to classify bioreactors is by the state of reaction sites, whether they are immobilized or suspended in the medium [Eri09]. Industrial bioreactors are available in sizes from 10 to 20000 L. They are also classified based on their lifetime as reusable bioreactors and single-use bioreactors. Recently, single-use bioreactors have gained popularity due to their low cost and ease of up-scaling. Industrial bioreactors are available in various sizes, from the small scale of tens of litres to a capacity of 4000 L [Moo11]. The main focus of this study is on bioreactors used for mammalian cell culture.

2.1.1. Stirred Tank reactors and Scale-up

The most commonly used reactor type in the biopharmaceutical industry is a Stirred Tank Reactor (STR), which is used for the production of various biobased pharmaceuticals using mammalian cell lines like CHO cells. A stirred tank reactor (STR) or also commonly known as a Continuously Stirred Tank Reactor (CSTR), has a reaction vessel, a stirrer or an impeller which is driven by an external motor, an inlet for gassing, vertical baffles along the wall of the reaction vessel to prevent large vortex formation of the media and multiple ports and openings for feeding, draining and sensor installation. These reactors are designed to provide specific and controlled conditions to achieve the highest productivity. Cell lines such as CHO cells have a complex relationship with the various variables inside the reactor [Li10, Mac22, Sma22].

Controlling all the variables and maintaining a homogeneous reac-

tor mixture is a difficult effort made more difficult by the scale-up of the reactor size, which raises the operating volume of the reactor. The scale-up of the reactors requires an accurate transfer of processes and parameters developed on a laboratory scale to an industrial scale. The most common method for the scale-up of bioreactors is to keep some, if not all, the mixing parameters the same between reactor sizes. The average specific energy dissipation rate, given by equation 2.1, is the most commonly used parameter for the scale-up of STR, which is the most commonly used reactor for fermentation and cell culture [Ama04, Moo11].

$$\epsilon_\theta = P/(\rho_L.V) = (Ne.n^3.d^5)/V \tag{2.1}$$

This is difficult to achieve because the scale transition does not translate linearly with non-linear changes in reactor geometry, non-linear reaction kinetics, non-linear mass and/or heat transfer kinetics [Gau23]. Thus, the culture milieu between the laboratory, pilot and industrial scales will unlikely remain the same throughout [Lar06]. In bioreactors, these scale-up variations and one of the methods of quantifying mixing by means of mixing time may be prone to unidentified heterogeneities in variables like dissolved oxygen, pH, and nutrient concentration. In many cases, this results in the cells moving from one concentration gradient to another, which may have detrimental effects on the cells. Heterogeneous zones and compartmentalization phenomena cause these localized concentration gradients [Gau23, Ros18, Fit21].

The following subsections discuss how heterogeneities can occur and affect the production in a bioreactor and the various sensor systems employed in bioreactors.

2.1.2. Inhomogeneity

As the demand for products produced via bioprocesses, like therapeutic proteins, enzymes, vaccines, etc., increases, there is a trend towards larger bioreactors with different mixing behaviours depend-

ing on the reactor type. The six main types of bioreactors used in industry are Continuous Stirred Tank Reactor (CSTR), Bubble column reactor, Airlift reactor, Fluidized bed reactor, Packed bed reactors, and membrane reactors [Moo11]. These reactors are used for the culture of various cell types like bacilli (Bacteria), Aspergillus (fungi), and Chinese Hamster Ovary (CHO) cells (mammalian). The mixing behaviour depends on the reactor shape, the type and configuration of the impellers, and the configuration of baffles. Especially the impeller design, which has the greatest impact on the flow behaviour of the fluid in a Stirred Tank Reactor (STR). The most commonly used impeller configurations are Rushton turbine and Pitched blade impellers, which have various flow patterns, which are shown by Bisgard et al. in fig 2.1 [Bis21].

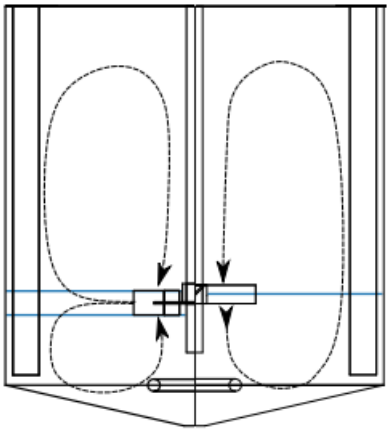

Figure 2.1.: Flow pattern comparison between Rushton Turbine (Left) and Pitched blade impeller (Right) flow patterns in a stirred tank reactor [Bis20]

The reactor design and scale-up objective is to keep every part of the reaction mixture homogeneous. This tends to get more complex

as the size of the reactor increases, as there is a possibility of stagnant or heterogeneous zones forming within the reactor. There is also the formation of compartments in the reactor, where it is delayed or no mixing. These inhomogeneities are more obvious in stirred tank bioreactors with aeration and a functioning two-phase system. These two-phase systems have higher numbers of inhomogeneities due to the complex hydrodynamic behaviour and interactions between various forces like buoyancy force, shear forces etc., [Ros18, Hof22]. This effect is shown in fig.2.2.

The heterogeneous region's impact on the cells relies on the gradient in concentration between the two zones that the cells move through. Still, it is more influenced by the length of time that the cells spend in the zone of heterogeneity [Bru17].

The effect of heterogeneous regions on the reactor's productivity is due to quorum sensing, which communicates between cells using small signalling molecules called autoinducers. This phenomenon is linked to apoptotic, necrotic and autophagic phases in the cell life cycle. Thus, Quorum sensing greatly influences cell division, gene expression and cell death, thereby impacting a bioreactor's productivity. Due to heterogeneous regions, some cells that stay stagnant in these regions may release more autoinducers specific to that region's conditions, which, when mixed with the entire reactor volume, may cause undesirable consequences. This is important in determining the reactor performance and the final quality and quantity of the final product [Shr06, Cho07].

Heterogeneous regions can be caused by the addition or change in concentration of one or more substrates or when the flow regime is changed in the reactor. In a two-phase mixing process in a 15000 L STR, heterogeneous zones occur under two distinct flow regimes: loading and flooding (fig 2.2). These heterogeneous regions influence the scale-up and performance of reactors by influencing the mixing parameters and the distribution of substrates and causing stagnant zones in the reactor. Due to their influence on the scale-up properties and productivity in the bioreactors, these in-homogeneities are being closely examined [Ros18]. This is achieved using a variety

of techniques, such as the use of sensors, simulation, and pilot-scale reactors. [Kus20].

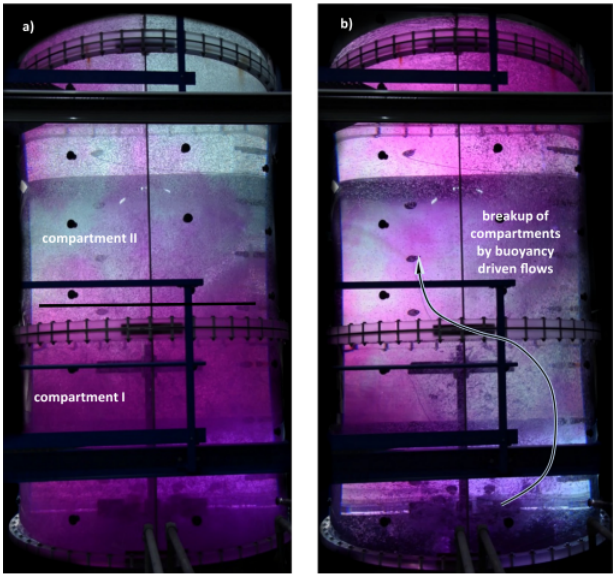

Figure 2.2.: Heterogeneous regions formed in a 15000 L STR in two flow regimes ((a) loading (b) flooding) during the two-phase mixing process after $t = 0.5(t_{mix})$. [Ros18]

2.1.3. Reactor Characterization Methods

In this subsection, the various ways used to study the fluid dynamic characteristics of a reactor are described.

Eularian sensor approach

The most commonly used method to determine the characteristics of a reactor is the sensors that are fixed to the reactor's walls via ports in

the reactor. These sensors use the Eulerian 1D method of measuring process conditions, which uses a stationary point of observation and fluid moves via or surrounding the relevant unit [Tro07b]. Although this is the most common sensor approach to measure the process variables in the industry, they have their own drawbacks. Due to the fixed position of the sensor, a measurement bias can be created as the results from a single or few selective points may not be adequate to represent the entirety of the reactor volume. This intensity is stronger in large-scale reactors, resulting in discrepancies between the cells' actual and measured process conditions. These inconsistencies occur due to the formation of local heterogeneities and the occurrence of compartments within the reactor volume. The heterogeneous regions thus formed may sometimes be completely undetected by the Eulerian sensors. To overcome these difficulties, other methods are used to study the bioreactor. One of them is using the decolourisation method.[Ros18, Hof22].

Visual Tracking approach

The visual tracking approach uses an indicator that changes colour based on the variable that is being studied. The most commonly used variable and indicator is the pH, which is very important for mammalian cells and must be kept within a specific range. A glass or acrylic reactor vessel is used to capture the colour change from the outside. The colour change is induced by adding a compound to the reactor that simulates an external feed to the reactor or a change in the process conditions. The drawback of this method is that such transparent reactors are available only for laboratory or pilot scale plants and are not usable in industrial settings due to various factors like cost, handling and re-usability etc. They are useful in studying a cell's respective "Lifeline" in an STR [Lap04, Rei12, Hof22].

Lagrangian measurement approach

To overcome the challenges of the characterization of large STRs that cannot be accurately studied or observed by the above-mentioned methods, researchers have begun to investigate the Lagrangian measurement approach. The Lagrangian measurement method involves tracking individual particles or observed volumes subjected to a flow field. This approach is realized using various sensory devices housed in a housing unit, which can move freely within the STR under observation [Lap04, Rei12, Lau19a, Bis20]. This method for studying these phenomena using Lagrangian Sensor Particles(LSPs) is described in the following section.

2.2. Lagrangian Sensor Particles

Lagrangian Sensor Particles (LSP) are mobile sensors in the bioreactor fluid housed in a housing unit and are kept so that they are neutrally buoyant in the reactor fluid. Their trajectory in the reactor is characterized by their shape, size, density, and buoyancy behaviour. They are designed to detect the spatiotemporal parameters in a reactor, especially in places where the conventional sensors, limited to the reactor walls, cannot reach. LSPs also try to mimic the cell movement and follow the cell life cycle in a bioreactor. This allows the monitoring of crucial changes in the bioreactor that cannot be measured employing fixed sensors, an example of this phenomenon is shown in fig2.3, which shows the sensor devices will be carried around with the liquid flow and measure relevant variables that potentially represent what microorganisms would experience when travelling throughout the volume. The measured values may deviate from the normal operating range in certain zones of the reactor volume. [Bis20, Rei15, Bun19]. The following sections elaborate on the few mobile sensor particles in development and the work done on their tracking.

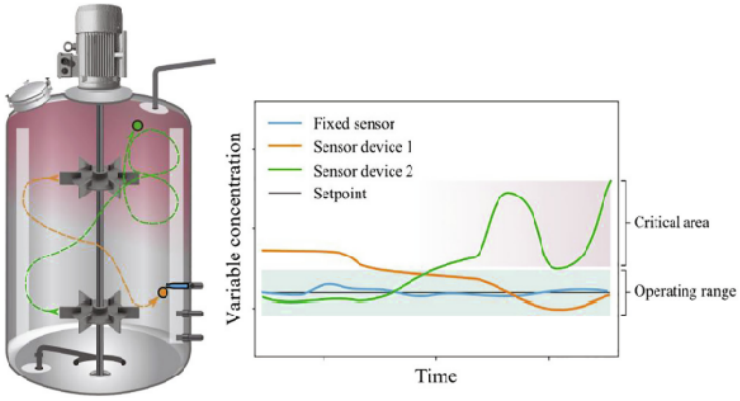

Figure 2.3.: Illustration of using Lagrangian Sensor Particles in a large-scale stirred tank bioreactor. [Bis20]

Mobile Sensor Development

The initial concept of mobile sensors was developed for the medical field and used to track the digestive system's internal working and problem identification. These sensor particles were called the radio pills [Wat62]. In recent years many teams have developed LSP to monitor the system inside a bioreactor. Table (2.1 lists a few prominent LSPs developed over the last decade. In most of these cases, the LSPs are equipped with an Inertial Measurement Unit (IMU), which in theory, allows for the mapping of the position of the IMU in the STR, using the acceleration data from the IMU and the initial position of the sensor. Another more commonly used sensor in the LSPs is the pressure sensor, which yields hydrostatic pressure. This can be used to determine the axial position of the LSP [Rei12, Zim13b, Lau19b, Cab21].

Table 2.1.: Various sensor particles developed over the years

Group	**Particle Diameter**	**Sensor Types**	**Year and reference**
Reinecke et al.	45 mm + variable length	Temperature Sensor, Pressure sensor and Magnetometer	2012 [Rei12]
SmartPART with Zimmerman et al	25 mm	IMU	2013 [Zim13b]
Stewart et al and Wand et al	28 mm	Temperature sensor and LED	2016[Ste15]
Stine et al	60 mm	Dissolved Oxygen sensor	2019 [Sti19]
Lauterbach et al	43 mm	ISFET pH sensor and Pressure sensor	2019 [Lau19b]
Cabrera et al	40 mm	6-Axis IMU	2021 [Cab21]
Kamp	20 mm	LED	2022 [Kam22]

Thiele et al.

One of the modern LSP in the last decade was developed by Thiele et al., which was developed for temperature and pressure measurements in large biogas reactors [Thi09]. This prototype LSP design has temperature, pressure and a 3D accelerometer. This was used for the measurements in a large reactor of 1.5 m diameter and 0.8 m height,

and the results obtained are shown in fig 2.4. The LSP measured the change in depth, temperature and raw 3D acceleration with respect to time in the reactor.

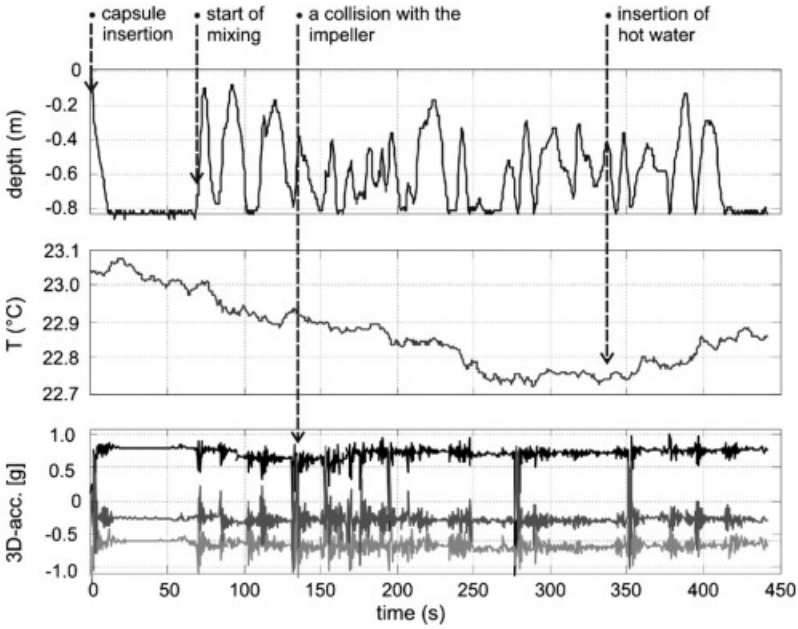

Figure 2.4.: Illustration of the data series recorded for the immersion depth, temperature, and 3D acceleration during the flow experiment in the reactor model by Thiele et al. [Thi10]

Reinecke et al.

The prototype developed by Thiele et al. was further improved and used by Reinecke et al. (Helmholtz-Zentrum Dresden-Rossendorf, Fraunhofer-Institut für Keramische Technologien und Systeme) to study the process conditions in 1000 L vessels. The LSPs are cylin-

drical in shape and have a variable density using a piston assembly. The sensor is fitted with a 3D IMU, a Pressure sensor, and a temperature sensor, and the general internals of the LSP can be seen in fig.2.3. This LSP is one of the first fully functional submersible sensor particles that can operate in a bioreactor. [Rei12, Rei16]. The code for tracking the position and velocity of the mote using the IMU is still being developed by Buntkiel et al. [Bun20].

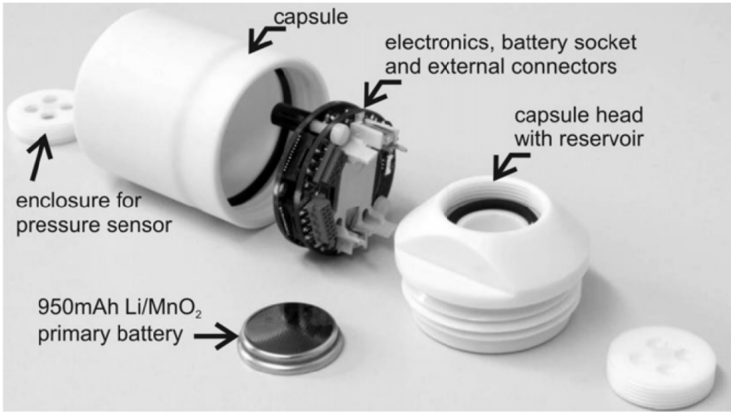

Figure 2.5.: Internal View of LPS developed by Reineke et al. [Rei12]

Zimmerman et al. (smartPART)

In the following years, various other LSPs were developed. The smartPART shown in fig.2.4 was designed by smartINST S.A.S., which is a startup situated on the ENS de Lyon campus. and used by Zimmerman et al. for analysis. This smartPART has a 3D IMU that transmits the data through a wireless transmission system, is 25 mm in diameter, and was used to measure flow patterns and Lagrangian acceleration patterns [Zim13b].

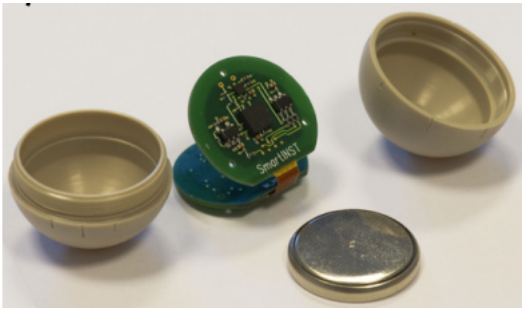

Figure 2.6.: smartPART developed by smartINST S.A.S [Zim13b]

Fig 2.7 shows the Probability Distribution Function of the translational acceleration results from data obtained by Zimmerman et al. using the smartPART. From these results, the different flow regimes variations, notably with large vortex formations, were documented. The three vertical lines indicate the saturation of one or two accelerometer axes and gravity [Zim13a].

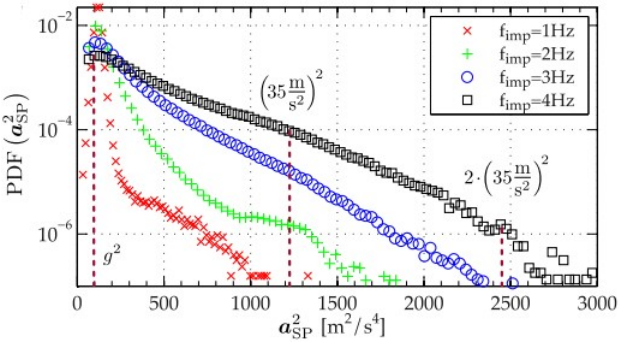

Figure 2.7.: A_{trans} PDF moments at various impeller frequency [Zim13a].

Stewart et al., Wang et al. and Kamp

The Instrumented Particles (IPs) developed by Stewart et al. with Wang et al. (fig 2.8) and a similar one developed by Kamp et al. (fig 2.9) are developed to study the motion of the fluid using visual methods. These instrumented particles have LEDs that can be detected using a camera. Then the recorded videos can be analyzed for velocity, position distribution, and fluid flow behaviour in the reactor [Ste15, Wan16, Kam22].

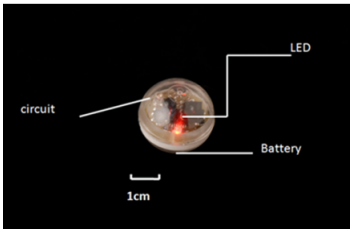

Figure 2.8.: Instrumented Particle designed by Stewart et al. with LED supported on a custom circuit [Wan16, Ste15].

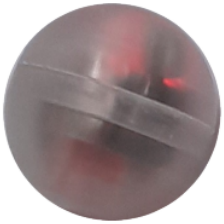

Figure 2.9.: Instrumented Particle designed by Kamp equipped with an LED and batteries [Kam22]

The results from trials by Stewart et al. are shown in fig 2.10 and fig 2.11. Fig 2.10 shows the mapping of the X, Y and Z coordinates

of the Lagrangian Particles with respect to the reactor vessel over a period of about 70 sec. The reactor vessel used is a glass beaker, and the two LSPs are blue and red in colour. A perturbation is induced into the system by adding water at a higher temperature than the system water after 34.4 s of the recording start. This led to a different pattern of movement of the LSPs which may be associated with the change in the fluid density and the disturbance caused by the action of fluid addition. Data on temperature measurements that were obtained simultaneously is also displayed. The disruption causes a shift in temperature that is clearly visible. The data from the Blue and Red capsules are displayed in the appropriate hues. [Ste15].

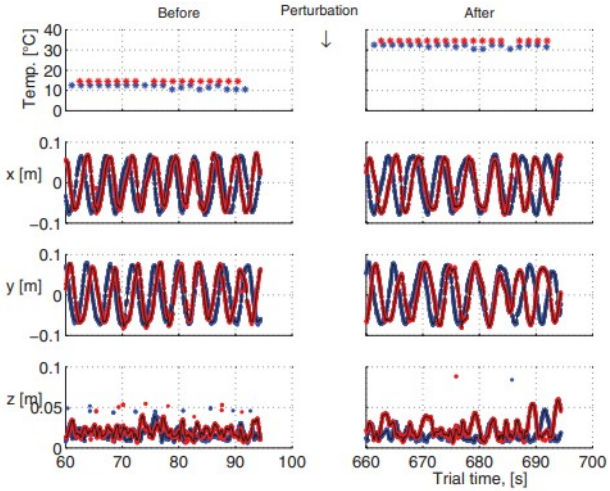

Figure 2.10.: Figure shows data from Stewart et al., where the x, y, and z-axis components for the recorded interval (34.4 s) before the perturbation and for the recorded interval (34.4 s) following the perturbation. [Ste15]

Fig 2.11 shows a small section of the reconstructed trajectories of the IPs before the perturbation. The median filtered result (solid line) is displayed with the data points (red and blue dots). Black squares mark the starting points of the data packets that were received during the interval that was recorded. There is also a data point not from the IPs but due to the reflection on the reactor wall [Ste15]. The IPs shown in fig 2.6 were also used in a similar experiment. The reactor used was a larger 200 L reactor, and only the front plane of the reactor was recorded.

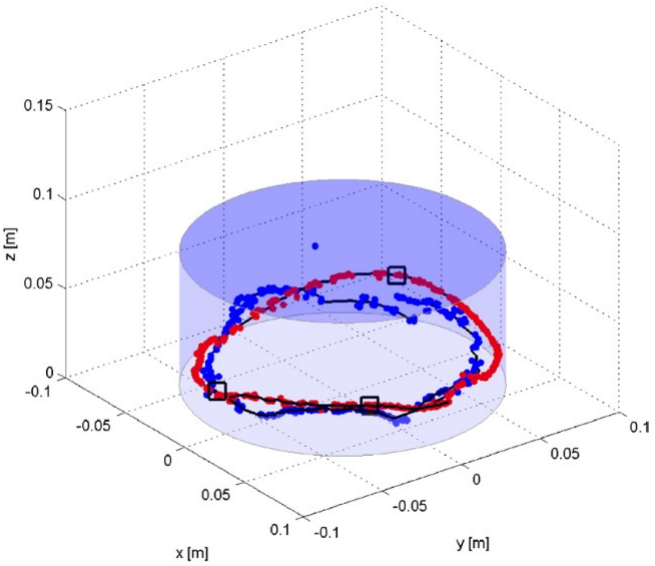

Figure 2.11.: Results from Stewart et al., showing approximately 4 s of the reconstructed trajectories for the blue and red capsules before the perturbation [Ste15].

Similar IPs and Capsule Tracking Velocimetry (CTV) to Stewart et al. were used by Wang et al. for a larger reactor, and the results

are shown in fig 2.12, where (a) 3D data points show the measured positions of the capsule. The same data is displayed top-down in (b), and (c) shows the median filtered outcome of the reconstructed particle route. The trajectory's individual x, y, and z axes components are shown as a function of time for a longer time period (almost 35 s) in (d). The data points were collected throughout a 70-second period. Raw data points are shown as red dots, while median-filtered findings are shown as black lines [Wan16].

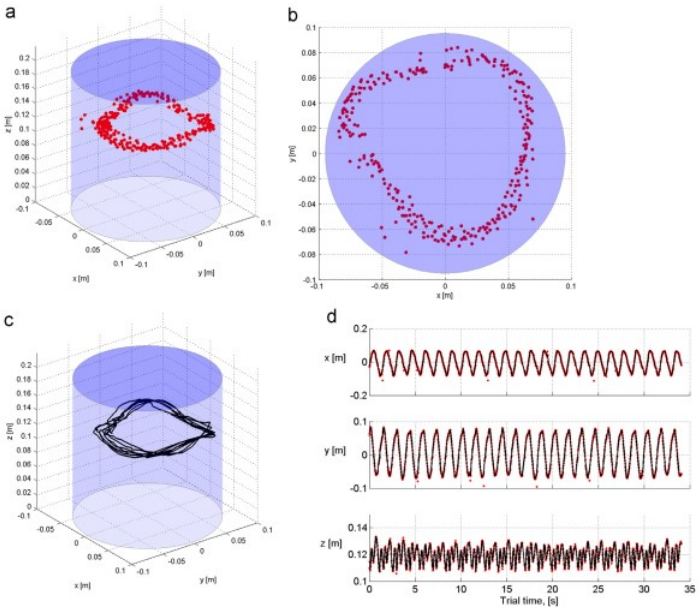

Figure 2.12.: Results from Wang et al., with particle tracking utilizing the CTV system developed by Stewart et al. [Wan16].

The LSPs developed by both Stewart et al. and Kamp are examples of Lagrangian Particles that have no sensors and are only for visual

tracking velocimetry (VTV) or CTV. Despite being extremely helpful in analysing the motion of large particles like LSPs in a reactor, they cannot independently measure system factors like temperature, pH, etc. Additionally, because these tests used a statistical technique and had observation times of fewer than 200 seconds, there may be less reason to be confident in the results.

Lauterbach et al.

The "Sens-o-Spheres" as seen in fig.2.13, which are developed by Lauterbach et al., are mobile temperature sensor in a shell of 7.9 mm diameter and can transmit data using a wireless method and was tested in shaking flasks, laboratory scale STRs and tube reactors in typical laboratory scale reactors (2L - 20 L). In all cases, the spheres showed reliable data transmission despite the potentially shielding technical environment like the interference from the reactor media, the reactor walls, impeller, motor etc. This may have been due to the smaller size of the reactor, as the amount of interference is directly proportional to the thickness of the obstruction between the source and the receiver. [Lau17, Lau19a, Lau19b, Pat06, Tas21].

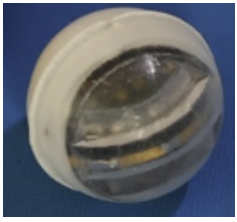

Figure 2.13.: Sens-o-Spheres by Lauterbach et al [Lau19a]

Bisgaard et al.

The LSPs, "Fermsense 3D" (fig.2.15, developed by Freesense ApS, are equipped with a temperature-measuring thermocouple, an absolute

pressure sensor, and an ISFET pH sensor built in a shell of 45 mm in diameter. These LSPs were used in reactors of different sizes to resolve axial flow parameters and mixing and circulation time calculations etc., an example of which is shown in fig 2.14 Along with computational Fluid Dynamics to simulate the particle distribution over the reactor by Bisgaard et al., the results from these experiments are discussed in further sections [Bis20, Bis21, Tas21].

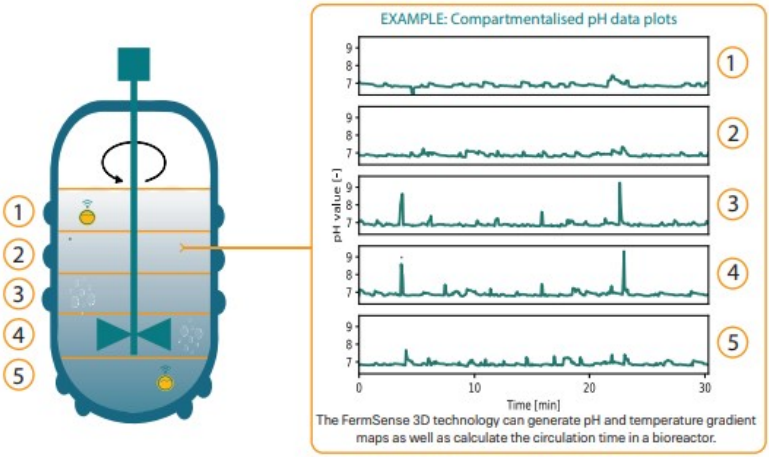

Figure 2.14.: Representation of compartmentalized pH data plots that can be detected using Fermsense 3D [Bis20]

Figure 2.15.: Fermsense 3D developed by Freesense ApS [Bis21]

Stine et al.

The bPod, as seen in fig.2.16, was developed by Stine et al. The goal was to create a sensor device for measuring DO gradients during pharmaceutical manufacture at scale in stirred bioreactors. A 60 mm-diameter device called the bPod was created with a Clark-type electrochemical dissolved oxygen sensor built into it along with Bluetooth for data transmission. For determining the DO percent saturation within a range that fits mammalian cell culture, the Clark-type sensor uses chronoamperometry. Chronoamperometry is a time-dependent method in which the working electrode is given a square-wave potential. As an analyte diffuses from the bulk solution towards the sensor surface, the current of the electrode, measured as a function of time, varies. Thus, the current-time dependence of the diffusion-controlled process taking place at an electrode can be measured using chronoamperometry, which is affected by the analyte concentration. This ISP was validated in a 2 L reactor and a 10 L reactor and revealed a linear current response to dissolved oxygen concentration [Sti19, Guy16].

Figure 2.16.: bPod developed by Stine et al [Sti19]

Over the course of 1.5 hours, the gas supply is alternated (O2:N2 - 100:0, 75:25, 50:50, 25:75, 0:100) using a 5-minute measurement interval. Every 10 seconds, which is the amount of time needed for the reactor to attain a steady state, the voltage output from the bPod was recorded. The data was also compared with the data from a fixed DO sensor. The results are shown in fig 2.17. The study's findings for DO measurements in sensor devices were encouraging. But this early version was still plagued by a sizable sensor drift and a brief sensor lifespan. [Sti19, Bis20].

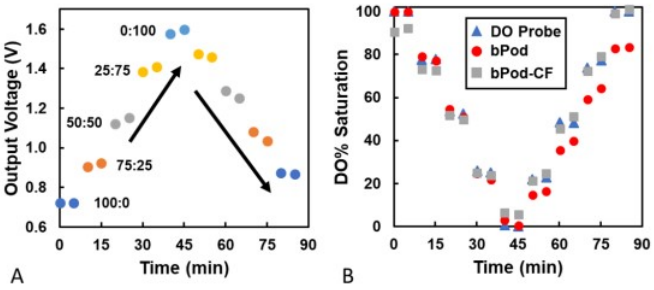

Figure 2.17.: (A) Electrochemical behaviour of a mobile bPod with batteries in a 10 L bioreactor. (B) The inline DO probe (blue, triangle), the bPod (red, circle), and the corrected bPod (bPod CF) are contrasted [Sti19]

Cabrera et al.

The LSP developed by Cabrera et al. (fig.2.18 has a 6-axis IMU, and the data is recorded on a Secure Digital (SD) card. The LSP is used to study the Lagrangian characterization of turbulent free surface flows [Cab21].

Figure 2.18.: LSP developed by Cabrera et al., [Cab21].

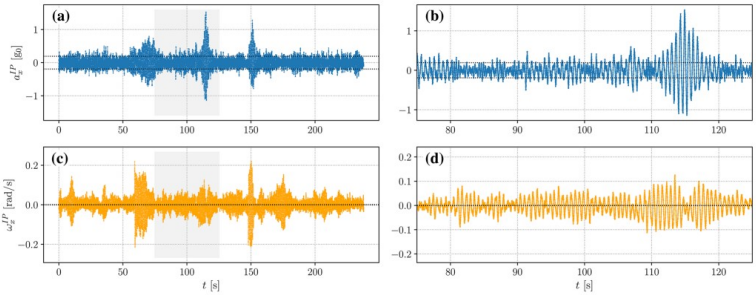

Figure 2.19.: Time series of the LSP's measurements of translational acceleration (top row) and angular velocity (bottom row) for experiments on gravity wave turbulence, acquired at a sampling frequency of 100 Hz for a forcing amplitude of A = 15 mm. [Cab21].

These LSPs were used to measure the turbulent free-surface flows.

The surface waves were simulated by partially immersed paddles controlled by servo motors. The results are shown in fig 2.19 and fig 2.20. In fig 2.19, the translational acceleration and angular velocity from the X-axis are plotted against time for simulated gravity waves. Only the X component is displayed; the other axes registered qualitatively similar behaviours. Within the 50 s time window highlighted in grey, panels (b) and (d) display a zoomed view of the time series shown in (a) and (c), respectively. A dotted (black) line in the panels designates the root mean squared (RMS) values for the translational acceleration and angular velocity parameters.

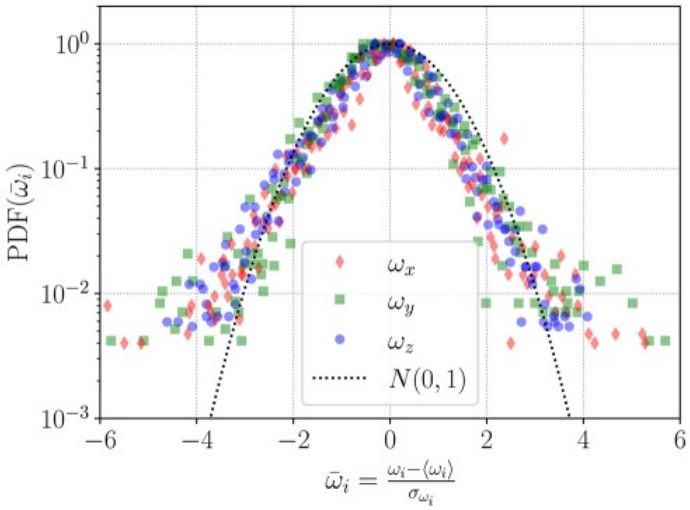

Figure 2.20.: Probability density functions for the largest considered forcing amplitude (A = 20 mm) for the angular velocity (normalised) recorded by the LSP. [Cab21].

In fig 2.20, Probability Distribution Functions (PDF) for the angular velocity are shown. Data are shown with markers: (red)

diamonds, (green) squares and (blue) stars denote the x, y, and z axes, respectively. The standard normal distribution is depicted by a (black) dashed line as a reference [Cab21]. The instrumentation design of this particle has inspired the Lagrangian Sensor Particles in this study.

2.3. Sensor Tracking

Though Lagrangian Sensor Particles have the advantage of being mobile and free-flowing over the more traditional sensors, the spatial resolution of the particles is being researched to determine the flow-following behaviour and trajectories of the particles inside the fluid. The flow-following behaviour of the sensor particles depends on the density and geometry of the sensor particles, the geometry of the reactor, the apparent density of the fluid of the reactor and the impeller setup in the reactor. The apparent density is the density of the fluid in an aerated reactor and is given by $\rho_{app} = (1 - \epsilon)\rho_l - \epsilon\rho_g$, where ϵ is the volumetric gas holdup, ρ_{app} is the apparent density, ρ_l is the liquid density, and ρ_g is the gas density. Since the gas density is much smaller than the liquid density, it can be ignored. This affects the floating behaviour of particles of the same density. For particle densities that are neutrally buoyant in only liquid, particles smaller than the bubble diameter will experience only the liquid density and the particles larger than the bubble density will experience the mean density of the mixture. This phenomenon dictates that LSPs must be as small as possible to avoid being affected by aeration in the medium. [Hof88, Mid79, Bis20].

The spatial resolution is necessary for the Lagrangian measurement method as Lagrangian measurements depend on two factors. The first is the ability of the sensor to move with/within the fluid it is sensing. The LSPs solve this. The second is the spatial resolution of the sensor with respect to the reactor, which is the determination of the coordinates of the LSP in the reactor during the measurement [Bun20, Lau19a, Bis20].

This has been done by various methods, like using (Inertial Measurement Device) IMU or the axial position measurement using hydro-static pressure measuring devices [Rei16, Bun20]. Lauterbach et al. were able to determine the maximum density of spheres that could still be evenly dispersed within a reactor by using Computational Fluid Dynamics (CFD) simulations. [Lau19a]. Other special methods have been proposed, like installing a Bluetooth mesh network that allows for data multi-hopping between scattered sensor devices. As a result, using a low-power tracking technique that uses the Bluetooth signal strength using Received Signal Strength Indicator (RSSI) along with the magnetometer and pressure sensors built into the device, it would be possible to localise individual nodes without relying on an earlier LSP location. It is also possible to link an observed magnetic field to the separation between the sensor and a magnetic source using a magneto-resistive sensor, such as the LIS3MDL (ST Electronics) with dimensions of 2.0 mm x 2.0 mm x 1.0 mm [Meh12, Che16].

In the following section, the methods using IMU and pressure sensors are discussed.

2.3.1. Axial Flow Measurements Using Pressure Sensor

A Micro-Electro-Mechanical System (MEMS) pressure sensor, such as the LPS33HW (ST Electronics), is used for determining the axial position of a sensor particle using hydrostatic pressure. This can then be used to evaluate the axial position distribution, axial acceleration and velocity profile and their distribution. Reinecke et al. identified the axial position distribution using the Lagrangian Sensor Particle they developed. It revealed a correlation between the particle density ρ_P and the fluid density ρ_f. The LSP has a piston to control the density of the LSP, and three densities were used for the experiment, $\rho_P \approx \rho_f$, $\rho_P \approx .98\rho_f$, and $\rho_P \approx 0.94\rho_f$. The reactor fluid was water at a density of 998 kgm^{-3}, and the height of the reactor was 0.8 m. Three impeller speeds were selected 0.92, 1.23 and 1.53 $s^{\neg 1}$

corresponding to the Reynolds numbers $2.310_5, 3.110_5$ and 3.810_5. Thus keeping the reactor in the turbulent region. As shown in fig.2.21, from which we can infer that the axial residence profile of the sensor particle is directly affected by the density of the particle. At neutral buoyancy ($\rho_P \approx \rho_f$), the LSPs show a residence profile that characterizes the hydrodynamics of the process at lower density the particle tends to be in the upper regions of the reactor. At the lowest density ($\rho_P \approx 0.94\rho_f$), the LSP is almost always suspended near the top of the reactor [Rei12, Rei16].

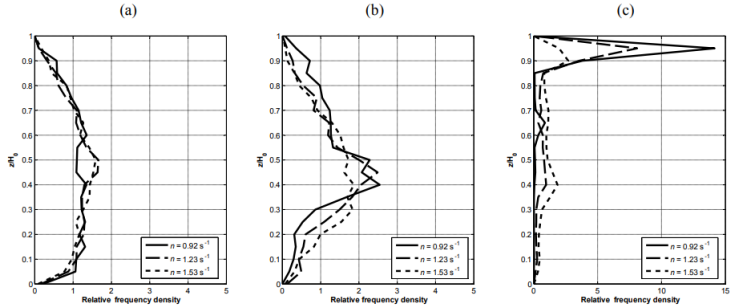

Figure 2.21.: Vertical residence profiles of the sensor particles from the experiments in the stirred vessel for characterization of the required density offset at the respective Reynolds numbers of $2.310_5, 3.110_5$ and 3.810_5 with different density ρ_P of the sensor particles at the fluid density ρ_f :(a) $\rho_P \approx \rho_f$, (b) $\rho_P \approx 0.98\rho_f$ and (c) $\rho_P \approx 0.94\rho_f$. [Rei16]

Further studies done by Bisgard et al. using a pressure sensor have also shown the correlation between the axial movement and two different impeller setups, namely the Rushton Disk Turbine (RDT) and Pitched Blade Turbine (PBT) impellers. These studies used "Fermsense 3D" developed by Freesense APS, shown in 2.22. The reactor employed in the study was 0.93 m in height and 0.93 m in

diameter, with an impeller diameter of 0.3 m for both the impellers used. It also had 4 baffles of 0.9 m in length. A down-pumping mixed-flow impeller (45 4-bladed pitched blade turbine, PBT) and a radial impeller (6-bladed Rushton disc turbine, RDT) were used for agitation. P/V levels used in the studies were 0.02, 0.11, 0.21, and 0.31 kW/m3 keeping the Reynolds number between $Re = 910_4$ to $Re = 410_5$.

Fig 2.23 shows the comparison between the axial movement over the normalized height of the reactor over a 120sec interval for the Rushton Disk Turbine (RDT) and Pitch Blade Impeller.

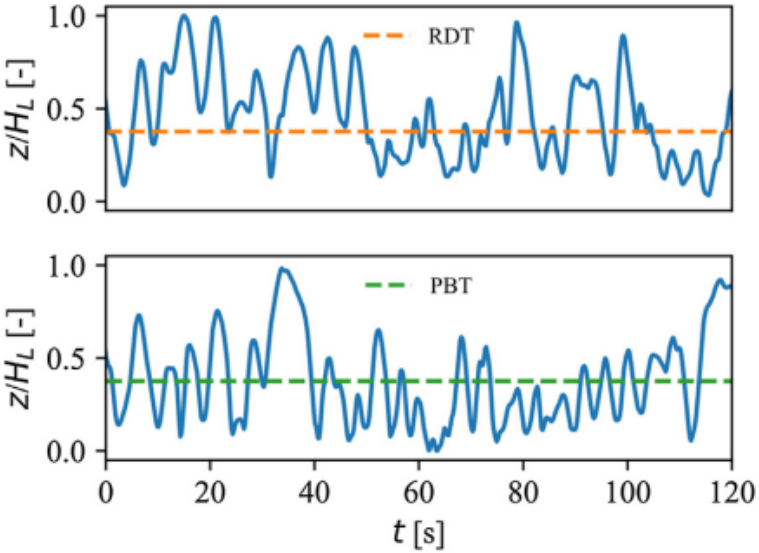

Figure 2.22.: An example of the axial movement of a sensor device using the RDT (top) and the PBT (bottom) at N = 105 rpm. The axial position has been normalized with respect to the liquid height. The dashed lines represent the impeller location [Bis21]

The study also tries to find the correlation between average axial velocity ($\bar{v_z}$) and normalized height (z/H_L) for RTD and PBT. The results from the PBT and the simulations are compared in fig 2.14. At lower P/V ratios, the experimental results match the results from the sensor. They diverge at higher P/V ratios, and this divergence is mostly located near the impeller and the top of the reactor. This can be due to the effects of the buoyancy and gravitational forces on the simulations [Bis21].

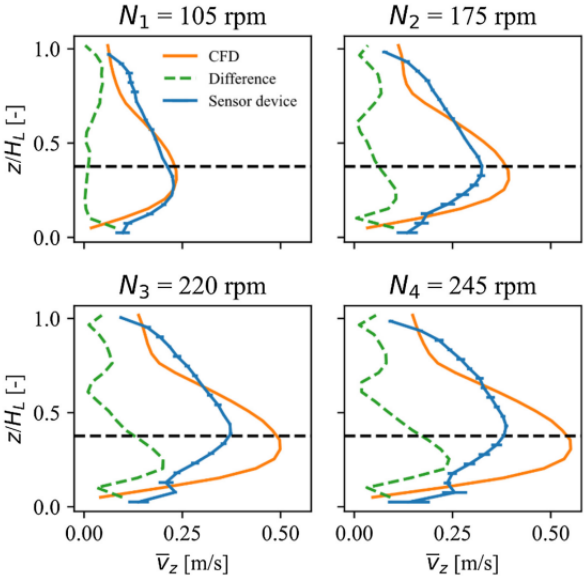

Figure 2.23.: Measured (blue) and simulated (orange) average axial velocities ($\bar{v_z}$) of the LSPs over the normalized liquid height (z/H_L) for the flow field generated by the PBT. The green dashed line represents the difference between the measured and simulated velocities. The black dashed line represents the impeller location. [Bis21]

Fig 2.24 shows the comparisons between the axial velocity profiles for RTD and PBT for various impeller speeds where $N_1 = 105$ rpm $N_2 = 175$ rpm $N_3 = 220$ rpm and $N_4 = 245$ rpm. It is seen that the LSPs have a higher axial velocity near the impeller for the PBT and a sharp decline in the axial velocity near the RDT. This is attributed to the flow patterns of the respective impellers.[Bis21].

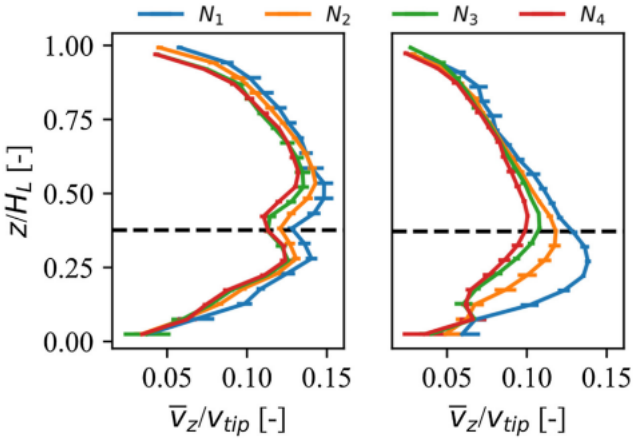

Figure 2.24.: Axial velocity profiles normalized to the impeller tip speed of the flow generated by the RDT (left) and the PBT (right). The dashed line indicates the impeller location. The error bars depict the standard deviation in $\bar{v_z}/\bar{v_{tip}}$ obtained from four individual sensor devices[Bis21]

2.3.2. Inertial Measurement Unit

Inertial Measurement Units (IMU) have been used since 1930 for aircraft navigation and navigation of other large objects. These IMUs were large devices and took up a considerable amount of space. The modern IMU is an electronic device based on the micro-

electromechanical system (MEMS) architecture, which makes it smaller, cost-efficient, energy-efficient and more precise than its mechanical counterpart. IMUs have an accelerometer that measures the inertial acceleration with respect to the earth's gravitational field. Some IMUs also have a gyroscope that measures the angular rotation, and this gives the IMU the ability to measure the roll, pitch and yaw, as shown in fig 2.25. The accelerometer and gyroscope have three degrees of freedom (DOF) to measure from three axes. A magnetometer can also be incorporated into an IMU. The magnetometer is used to measure the bearing magnetic direction. This helps in the improvement of the gyroscope readings.

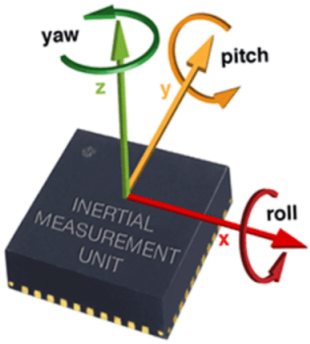

Figure 2.25.: Roll, Pitch and Yaw axis from an IMU sensor's perspective [Cho19].

IMU Types

An IMU can have just an accelerometer and is generally called a 3 DOF or 3D IMU like the one used by Reinecke et al. [Rei12]. An IMU with an accelerometer and a gyroscope is termed a 6 DOF or 6D IMU, like the one used by Cabrera et al., [Cab21]. The study done by Buntkiel et al. and this study used an IMU with an

accelerometer, a gyroscope and a magnetometer, which is called a 9 DOF or 9D IMU [Bun20]. The 9D IMU is the most advanced IMU currently available on the market, as the magnetometer works in tandem with the gyroscope to measure the yaw angle of rotation. This improves the drift issue of the gyroscope. When drift errors are minimal, this sensor performs well for short- and long-term dynamic orientation calculations. However, the inclusion of the magnetometer in the package has a drawback. The magnetic field disturbance may impact measurements if the IMU is utilised in an environment with ferromagnetic metal all around. This may be avoided by calibrating the IMU in the environment. Some IMUs have a microprocessor that helps in the auto-calibration of the sensor. IMUs can be used to determine movement in terms of acceleration, angular velocity and rotation. IMUs are most commonly used for navigation purposes, mostly in tandem with Global Positioning System (GPS) [Zhu04, Zha11, Ahm13].

A few examples of IMUs used in LSPs and the results obtained are discussed below.

Momentum and Flow Measurements using IMU

IMUs are integrated into some LSPs by groups like Cabrera et al., Bisgard et al., Zimmerman et al., Reinecke et al. and Thiele et al. The IMU in the LSPs measures the acceleration and velocity profiles of the particles in a fluid. The data can also be used the determine the flow following behaviour of the LSPs by finding the various dimensionless numbers like Stokes number, particle Reynolds number etc., [Cab21, Bis21, Zim13a, Rei16, Thi10].

The accelerometer data can also be used for the circulation time analysis by finding the acceleration magnitude, which is the unidirectional forces acting on the sensor particle given as

$$a_{mag} = \left(\frac{\sqrt{a_x(t)^2 + a_y(t)^2 + a_y(t)^2}}{g} \right) - 1 \tag{2.2}$$

where a_{mag} is acceleration magnitude, a_x, a_y, and a_z are the inertial accelerations acting on the sensor, t is the time in seconds, and g is the gravitational constant. In fig 2.26, the correlation between a_{mag} and different axial positions of the mote is shown for two different impeller setups, which shows a direct correlation between circulation time and acceleration magnitude [Rei12].

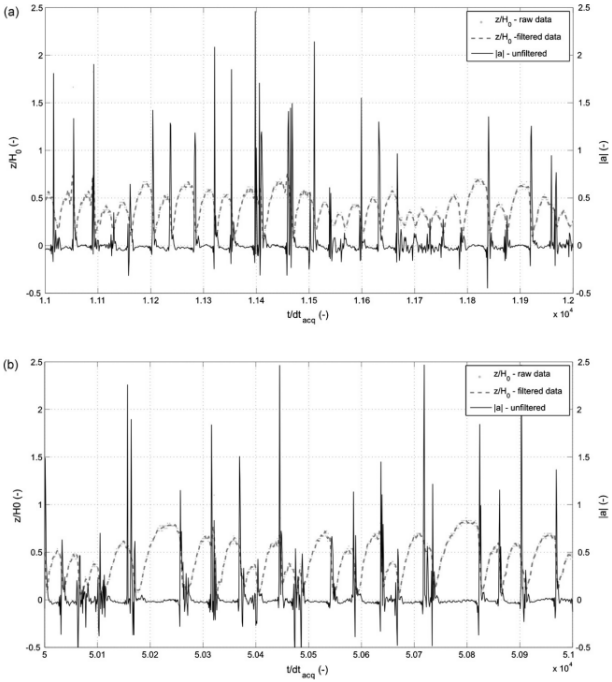

Figure 2.26.: Selected time sequences of 1000 measured values of z/H_0 and a_{mag} from the time series for both impeller positions (a) h_a and (b) h_b.[Rei12]

However, the raw acceleration data from the IMU cannot be used

for these calculations, as the sensor is not always steady inside the fluid and tends to spin and rotate. Thus the data that has been recorded from the sensor must be corrected for the attitude of the sensor with respect to the reactor. Attitude is the orientation of the IMU. For 9D IMUs, it is with respect to the Earth's magnetic and gravitational field. This uses an error state KALMAN filter which is discussed next [Bun20].

Kalman and AHRS filters

The acceleration data can also be used to find the velocity by doing a single integration and position of the sensor by double integration of the acceleration values. Still, this method has an issue with the gradual accumulation of errors leading to a gradual drift in the perceived position of the sensor. This gradual accumulation of error is known as dead reckoning. This can be compensated to a degree by using filters on the data like Kalman filters etc., [Wit19].

The drift error in the IMU is one of the main reasons the IMU is not used alone for positional tracking. This drift occurs from two sources. The first source is from the gyroscope on the IMU, and the second source comes from the integration error that comes from the calculation of position from acceleration data. The first error is compensated with data processing algorithms. The first of such algorithms was called Kalman filters. Since then, better filter versions have been developed [Kra03, Bun20, Dia15]. Kalman filters are predictive algorithms that determine the state of interest by observing the data related to its current state. It has been used for various applications like guidance and navigation, target tracking, and motion estimation [Kov13]. This study uses these filters for error correction in a post-process script using MATLAB code.

Buntkiel et al. used an error state Kalman filter (ESKF) algorithm to track the attitude of the sensor particles concerning reference coordinate systems. This algorithm could track the sensor's attitude even at high accelerations, which is generally difficult [Bun20]. But Kalman filters can only provide the attitude of the IMU. Modern

algorithms based on Kalman are used to refine the data further. These are called Attitude and Heading Reference Systems (AHRS) filters. Two modern AHRS filters fuse gyroscope and accelerometer/-magnetometer readings Madwick AHRS and Mahony AHRS.

The Madgwick system, based on a gradient descent optimisation of the relative 3D orientation of the IMU towards the gravitational field to be determined using accelerometer readings, and the orientation along the Earth's magnetic field is to be determined using magnetometers. By carefully weighing the contribution of each sensor, a parameter is employed to regulate the pace of convergence to the orientation estimation. The approach employs quaternion representation and numerical integration of the orientation data [Mad10].

The Mahony approach relies on an explicit complementary filter and calls for outputs from the accelerometer, gyroscope, and magnetometer. Its structure makes it appropriate for use with embedded devices. Additionally, it calculates the gyroscope biases. Mahony utilises a differential and integral controller, whereas Madgwick uses a proportional controller to correct the gyroscope bias [Mah08].

This study utilises the Mahony AHRS algorithm on MATLAB. The next chapter describes the design and construction of the LSPs used and the experimental setups in this study.

3. Materials and Methods

This chapter describes the Lagrangian Sensor Particle's (LSP) design, construction and working. In addition, the programs used for data processing and the data flow are described. Then, the reactors and their setup is described. This study uses two reactor setups: a 200 L reactor and a 15000 L reactor.

3.1. Lagrangian Sensor Particles

All the components in the LSP are off-the-shelf components that can be easily purchased and acquired. This is one of the objectives of this study. Two types of LSPs are designed for this study, one with an IMU and the second with a pressure sensor. They can be theoretically integrated into the same unit. Due to the type of microcontroller chosen, there is a limit to the size of the program that could be uploaded on the microcontroller. Thus only one sensor could work in the unit at a time. Both the sensors work on the same Inter-Integrated Circuit (I^2C) architecture. Commonly called I2C, and are interchangeable on the circuit diagram.

The LSPs work on an I2C architecture. In 1982, Philips Semiconductor (now NXP Semiconductors) created the I2C serial bus short-distance protocol to improve communication between the core on the board and numerous additional Integrated Circuits (IC) surrounding the core. All the components in the LSP are off-the-shelf components that can be easily bought. This is one of the objectives of this study. The LSP have a translucent shell made of Poly(methyl methacrylate) (PMMA), which is a transparent material, but due to the machining of the material, it becomes translucent. The spherical

shells are 40 mm in diameter and are identical for both sensor types. The circuit diagram is based on the one used by Cabrera et al. and has improved components and shell design to accommodate the use of the pressure sensor and Light Emitting Diodes (LEDs) [Cab21]. The size of the sensor breakout board limits the size of the shell, but it closely matches the LSPs used by other groups like Lauterbach et al., Reinecke et al. and Cabrera et al., which are all larger than or equal to 40mm in diameter.

The following subsections describes the various components used for the LSPs, followed by the circuit diagram and the development of the LSPs.

3.1.1. Inertial Measurement Unit (IMU)

The Inertial Measurement Unit(IMU) used in this study is a 9D or 9DOF IMU on an Integrated Circuit breakout board (IC board) from the manufacturer BlueDot GmbH (Fig 3.1). This uses an advanced IMU sensor BNO055 (Bosch). The BNO055 is a 9-axis smart sensor, which integrates a microcontroller and three orientation sensors (accelerometer, magnetometer and gyroscope) on a single chip. The BNO055 contains a triaxial geomagnetic sensor, a triaxial 16-bit gyroscope and a triaxial 14-bit accelerometer in a single package. This enables it to simultaneously measure the linear acceleration, rotational velocity and strength of the magnetic field experienced by the sensor in 3 directions.

Besides measuring acceleration, gyroscopic and magnetometer readings, the sensor can also provide orientation data in the form of Euler angles and Quaternion data. Euler angles explain the rotational orientation of a rigid body around its three axes. Roll angle (ϕ) (around x-axis), pitch angle (θ)(around y-axis), and yaw or heading angle (ψ)(around z-axis) are the angles that are indicated.The Euler angles are not the best for representing rotational direction because they suffer from Gimbal lock. A Gimbal lock is the loss of a degree of freedom in a rotation system. It will always happen in any system that uses Euler angles, which is caused by the rotation of the object

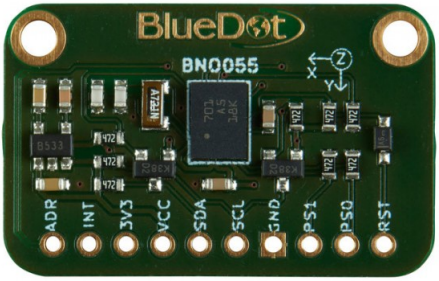

Figure 3.1.: 9 Axis IMU BNO055 by BlueDot [BNO17]

by applying a fixed set of successive rotations. [Kla17]. However, quaternions provide a different technique to define orientation or rotations in three-dimensional space, using an ordered set of four numbers. They are free of gimbal lock and can describe any three-dimensional rotation about any arbitrary axis [Gol11].

The fusion algorithm running on the onboard 32-bit microcontroller reads all the sensors simultaneously. It delivers data like the gravity field vector, the device's absolute orientation (through the quaternions and Euler vectors), and the magnetic north (as with a compass). The maximum recording frequency of the chip is 20 Hz which is limited by the magnetometer data. The maximum frequency is 100 Hz for accelerometer and gyroscope data. When only the acceleration and gyroscopic data are required, the chip can record at 100 Hz. Still, only a 20Hz recording frequency can be used when all three sensors' information is needed. The accelerometer ranges between ± 2 G to ± 16 G and has a 1 LSB/mG sensitivity at 25 °C, where LSB is the Least Significant Bit, and G is the gravitation constant. The gyroscope works in a range between 125 °/sec to 2000 °/sec with a sensitivity of 16.0 LSB/°/sec at 25 °C. The magnetometer has a typical range of ± 1300 μT in the X and Y axis and ± 2500 μT in the Z axis at 25 °C and a resolution of 0.3 μT.

The sensor can run on voltages between 2.8V to 5.5V and runs on an I2C protocol that needs only two connections for complete data communication with a default I2C address of 0x28. While most devices interpret 5V as logic HIGH, the BNO055 uses 3.3V as logic high, so the onboard logic level converter translates the 5V signals into 3.3V signals and vice-versa. Thus the sensor can run on low voltages and be power efficient. The board's architecture is given in appendix A. The LSP with IMU works at 20 Hz, making one recording every 50 ms [Bos14].

3.1.2. Pressure Sensor

The initial pressure sensor considered for this study is the MPRLS sensor by Adafruit Industries LLC, US. This is also an I2C-based system with two connections for data communication. Due to this being an outdated sensor and interface issues between the microprocessor and the chip and also due to it being very sensitive to static, this sensor is later replaced with another pressure sensor.

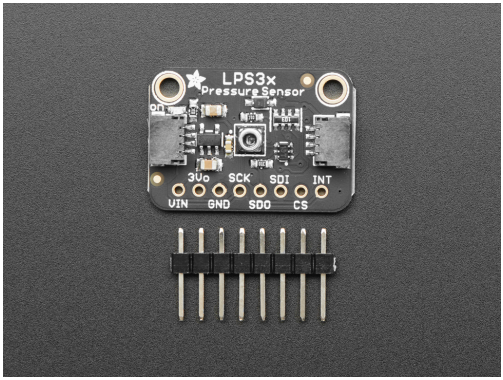

Figure 3.2.: LPS33HW pressure sensors by Adafruit Industries LLC [Ada19]

The pressure sensor used in this study is Adafruit LPS33HW, from the manufacturer *Adafruit Industries LLC, USA* (Fig 3.2, which is a hybrid sensor that has both pressure and temperature sensor. It works on I2C architecture. The actual sensor on the breakout board is from *STMicroelectronics N.V., Geneva, Switzerland.* The board's architecture is given in appendix B. The pressure sensor has a rated measurement range from 200 hPa to 1260 hPa (0.2 bar to 1.26 bar) absolute pressure range, and the temperature sensing range is from -45 to 85 °C. Its pressure sensor has a sensitivity of 4096 LSB/hPa and relative accuracy over pressure of ±0.1 hPa in the operating pressure range and at 25 °C temperature. This sensor can work at 1, 10, 25, 50 and 70 Hz recording frequencies. This sensor has higher stability than MPRLS, as it is more resistant to static. It cannot work in concert with the IMU as it runs on larger libraries which are provided for the sensor by the manufacturer of the chip. Thus the program that runs both the LPS and BNO055 is too large to work on an AT-Tiny85 (about 300 Bytes larger than the max space size). Therefore, to work with the LPS33HW pressure sensor, a second Lagrangian Sensor Particle is built. The LSP with this sensor has a recording frequency of 20 Hz. Still, the sensor has a limited selection of working frequencies, so it works at an effective measuring speed of 10 Hz. [STM17]

3.1.3. Microcontroller

The microcontroller is one of the most essential components. It controls the other instrumentation and measures the time using the *millis()* function that counts the time from activation in milliseconds. The microcontroller also stores the program on which the LSP runs. This program is based on C++ (appendix D) and is uploaded onto the microcontroller using an Arduino Uno.

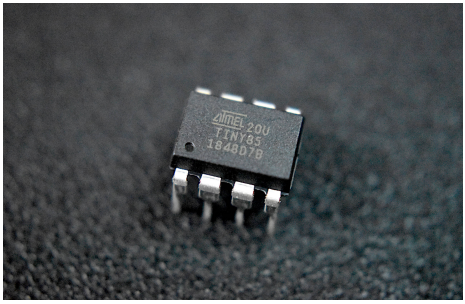

Figure 3.3.: AT-Tiny85 microcontroller

The microcontroller used is from the manufacturer *Microchip Technology Inc.* and is called AT-Tiny85 (Fig 3.3. The AT-Tiny85 combines 8 KB ISP(In-system programming) Flash memory for storing the program that runs the LSP, 512B EEPROM (electrically erasable programmable read-only memory) for loading the boot program to make the microcontroller function, 512B SRAM (Static random-access memory) for running the program during operation, six general-purpose I/O lines, one 8-bit timer/counter with compare modes, and one 8-bit high-speed timer/counter. The device achieves a throughput of 20 MIPS (Million instructions per second) at 20 MHz and operates between 2.7-5.5 volts. It also has an I2C channel.

In the LSP, the microcontroller uses 3 of its six general-purpose I/O lines for a serial clock pin (SCL) and the serial data line (SDA) for controlling the sensor chip. It has a Transmitter (Tx)/Receiver (Rx) pin for writing the data on the microSD card as an RX channel 3.6.

3.1.4. OpenLog

The component used for recording data on microSD (Micro Secure Digital) cards is SparkFun OpenLog by *SparkFun Electronics, Colorado, USA* (Fig 3.4), which is a data logger that works over a simple serial connection (RX/TX) and can support data cards of up to

32 GB capacity. It uses an ATmega328 running at 16 MHz and draws 2-3 mA of power when idle and 10-20 mA during recording, depending on the microSD card used. The OpenLog supports both FAT16 and FAT32 (File Allocation Table) formats. It can work at various logging speeds. In the LSPs, the logging rate is 115200 bps (bits per second). The logging rate and other aspects of the Datalogger are controlled by the *config.txt* file (Appendix F that is created automatically on the SD card when inserted into the Datalogger.

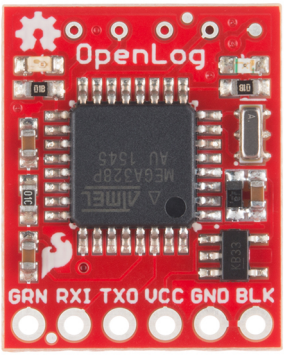

Figure 3.4.: OpenLog Datalogger by Sparkfun [Ope09]

3.1.5. Batteries, LED and Ballast

The batteries used are 290 mAh in capacity from KT Electronics. They are Lithium polymer batteries and are rechargeable. And interchangeable between the different LSPs by adjusting the ballasts. Ballasts are used to adjust the weight and change the LSP's buoyancy behaviour. The ballast is simple metallic fishing line weights wrapped with paraffin film to avoid contact with electrical parts and cause unwanted connections in the instrumentation. Each LSP also has two LEDs so the cameras can easily recognise them. There are three LED colours red, blue and green. The LEDs are connected to the

3V3 output of the sensor chip through a 220 Ω resistor.

3.1.6. Shell Design

The shells of the LSP are designed progressively and tested by 3D printing. The initial designs are based on the shell designed by Cabrera et al. and then are progressively improved to fit the sensors and other instrumentation. The final design is then made by Computer Numerical Control (CNC) machine and turning lathe Poly(methyl methacrylate) (PMMA). The material is transparent enough for the light from the LED to be visible. This is shown in Figure 3.5.

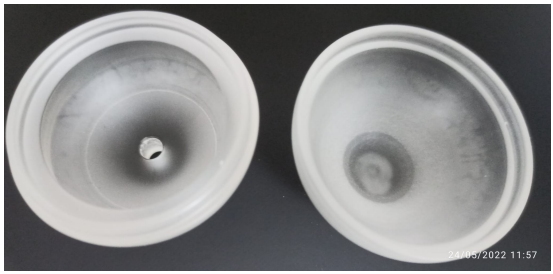

Figure 3.5.: Bottom (left) and top (right) half of the shell

The final shell design is 40 mm in diameter and has two hemispheres with one port in one of the hemispheres for the pressure sensor. The hemispheres are fitted together and sealed using transparent silicone paste that has to be applied and removed for every use. The same silicone paste is also used to seal the hose to the pressure sensor port. It also has a slightly protruding wall in the bottom hemisphere to stabilise the IMU sensor and prevent its sagging.

3.1.7. Circuit Diagram and assembly

The circuit diagram is the same for both sensor types, and this can further be upgraded to be modular as the sensor chip can be switched

to any sensor chip that works on an I2C architecture. The circuit is based on the work done by Cabrera et al. 2021. [Cab21].

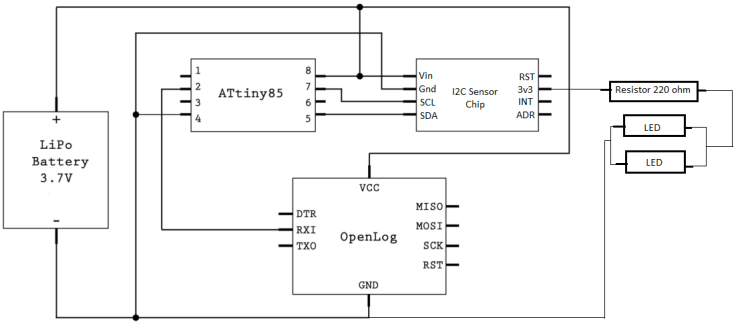

Figure 3.6.: General Circuit diagram

The sensor chip is replaceable as shown in the circuit diagram (Fig 3.6). Thus, the LSP is very modular, making it reasonably robust to any technological advancements for future upgrades. As the project aims to design an LSP from commercially available parts and show the feasibility of such a design, the circuit connections are based on a standard architecture that allows the replacement of one sensor with another sensor. Thus the two LSPs design developed for the project have the same circuit diagram. This modularity is due to the fact that the integration of the circuits is based on the I2C architecture. In theory, a custom-designed integrated circuit with multiple sensors can be used with the appropriate program to make the LSP multifunctional and upgradeable.

3.1.8. Inertial Measurement Unit (IMU) LSP

The layout of the IMU LSP inside the shell is kept so that the IMU sensor is as close to the centre of the spherical shell as possible. The microcontroller and the OpenLog are on one side of the IMU, and

the battery is on the other side (Fig 3.7). The ballast weights are kept near the microcontroller due to two reasons. First is space, as there is enough unoccupied space next to the microcontroller. The second reason is to distribute the weights evenly across the shell. As the battery is heavy, the ballast is put on the other side of the shell to compensate for that. All electronic components except the battery are connected to each other via external wires and are soldered. The batteries are rechargeable and removable from the circuit. It also acts as the power switch, as by connecting and disconnecting the batteries, the instrumentation can be powered on and off, respectively. The LEDs are placed near the centre on both sides of the IMU board. The instrumentation is not attached to the shell. Since the shell design for both LSP types is the same, the port for the pressure sensor on the shell is closed with acrylic glue for the IMU LSP.

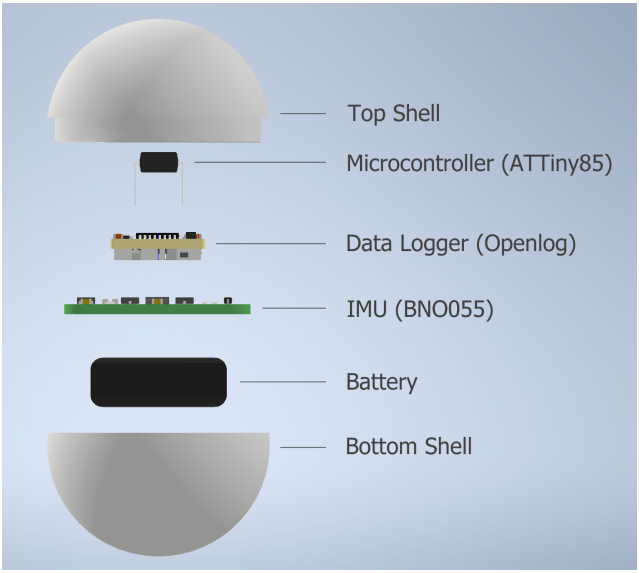

Figure 3.7.: IMU LSP layout

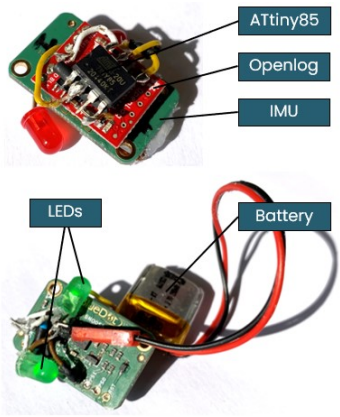

Figure 3.8.: Inertial Measurement Unit LSP with LED.

3.1.9. Pressure LSP

The pressure sensor's layout has been designed so that the pressure sensor is as close to the shell as possible, and the hose connecting the pressure sensor to the shell is as short as possible. The microcontroller and the data logger then followed the pressure sensor. The battery is attached so that it is in the other half of the shell. The data logger remains close to the centre of the shell and is placed in a way to make the microSD card easily accessible (Fig 3.9). The pressure sensor is attached to the shell via the hose using silicon paste to make the LSP water-resistant, thus making it feasible to detach the instrumentation for repairs or upgrades. The LEDs are placed next to the datalogger and kept as close to the centre as attainable. In this LSP, the ballasts are also placed next to the microcontroller for an even mass distribution due to space constraints.

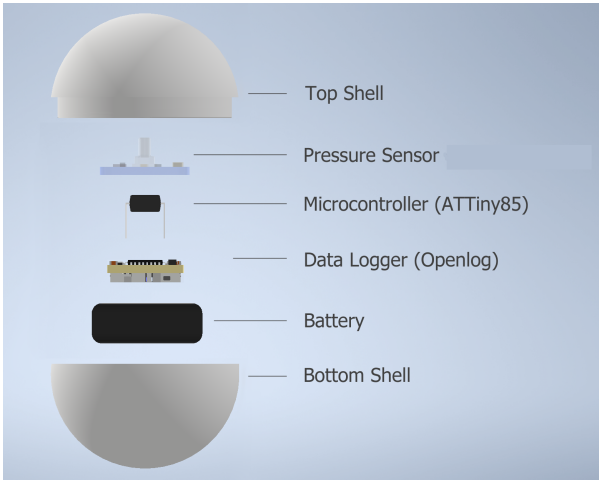

Figure 3.9.

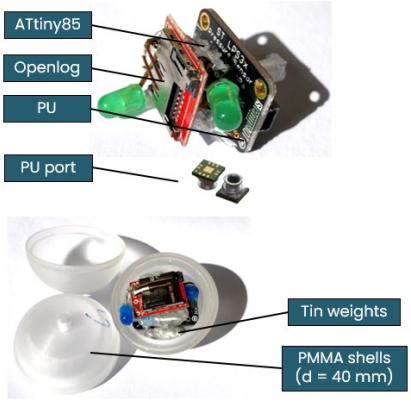

Figure 3.10.: Pressure LSP with LEDs

3.1.10. LSP program

The interaction between all the components in the LSP is governed by a program uploaded onto the microcontroller. This program is written in C++ and loaded onto the microcontroller using the Arduino UNO board. The circuit diagram for the connection from Arduino UNO to the AT-Tiny85 is provided in the appendix C.

IMU LSP

The program for the IMU LSP records the data to the microSD card in the format as shown in Fig 3.11.

Time (mills)	Acc X (m/s^2)	Acc Y (m/s^2)	Acc Z (m/s^2)	Gyro X (°/s)	Gyro Y (°/s)	Gyro Z (°/s)	Mag X (µT)	Mag Y (µT)	Mag Z (µT)	System Calibration	Accelerometer Calibration	Gyroscope Calibration	Magnetometer Calibration
1800	-1.56	9.28	-3.84	0.18	0.12	0.04	41.5	-35.38	42	0	0	0	0
1849	-1.47	9.19	-3.52	0.1	-0.22	-0.16	41.88	-35.06	44.06	1	3	0	0
1902	-1.39	9.2	-3.51	0.03	-0.18	-0.11	42.25	-35.06	44.38	2	3	3	0
1950	-1.64	9.19	-3.8	-0.12	0.08	0.16	42.56	-34.25	42.75	3	3	3	3

Figure 3.11.: IMU LSP output layout

The Program for operating the IMU LSP is given in appendix D. The output contains the time in milliseconds, the acceleration data is measured in ms^{-2}, the gyroscope data is measured as °/sec, and the Magnetometer data is measured as μT for all three axes relative to the sensor. Internal calibration data from the sensor follow this. Internal calibration data is a measure provided by the IMU to specify the degree of correctness of data. It ranges from 0 to 3, where 3 is the highest. The Euler and Quaternion data are not recorded as the AHRS algorithm (chapter 3.5.1) used for the data processing does not need it and derives these values through calculation.

Pressure LSP

The pressure LSP program is similar to the IMU LSP program, as seen in Appendix E. The only difference is the included libraries and

output data. Only the time in milliseconds, temperature in degrees Celsius, and pressure in hPa are displayed in the output. There is a delay in determining the real temperature of the fluid because the temperature sensor is on the board, and thus the heat is slow to diffuse through the tube and register on the temperature sensor. This is the reason the temperature data is not used in this study.

3.2. Experimental Setup

The LSPs are tested in two reactor setups. The first setup has a 200 L transparent reactor made of acrylic glass (PMMA) with an aeration hose and stirrer setup. It also has a cuboidal outer cover and a camera and mirror to get a possible 3-dimensional view of the reactor. The second is a 15000 L reactor which is also transparent and made of the same transparent PMMA. The experimental setup has been described in the following section.

3.2.1. 200 Liter Reactor and Setup

The reactor used in the 200 L setup is similar to the Biostat STR, *Sartorius Stedim Biotech(SSB)*, Germany. The acrylic glass container has a 200 L working volume. It has an inner diameter of 0.59 m, a height of 0.98 m, and a height-to-diameter ratio of 1.66. The bottom of the reactor is rounded to the left and right with a matching radius of 0.3m. The acrylic container is intended to resemble a single-use bioreactor commonly used in industry. The reactor's rounded bottom and smaller base than its top can be seen from the front. The side view of the reactor shows a cylinder with supports blocking a small part of the reactor (Fig 3.12). From the camera's point of view, the reactor front has a rounded bottom and is cylindrical at the top.

A larger cuboidal container that is filled with deionised water surrounds the reactor. The acrylic glass in this container prevents light refraction while reducing distortion. There is a 0.1 m gap between the reactor and the outside container. The stirrer in the

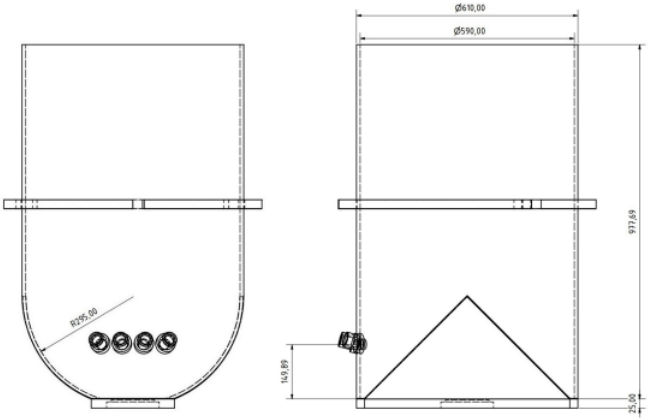

(a) Front view (b) Side view

Figure 3.12.: Schematics of the 200 L reactor

reactor has two different configurations and is powered by a motor at the top of the reactor. The Rushton Turbine and Pitched Blade impeller (PBRT) configurations have a Rushton Turbine at the bottom and a Pitched Blade impeller at the top. In contrast, the Pitched Blade and Pitched Blade (PBPB) setup has two identical Pitched Blade impellers, one above the other. The diameter of all impeller types is 22.5 cm, and the Pitched Blade impellers share the same design. The distance between the impellers is 0.3 m for both setups. The centre of the first impeller is 0.15 m from the bottom of the reactor, and the centre of the second impeller is 0.45 m from the bottom. The ratio of the impeller diameter (d_2) to the reactor diameter (d_1), $R_{d2d1} = 0.38$ for both impeller setups is given by the following equation. The reactor is the same as used by Kamp [Kam22].

$$R_{d2d1} = \frac{d_2}{d_1}. \tag{3.1}$$

For the experiments, four different stirrer speeds are used. The speeds are identical for both setups at 50 RPM, 70 RPM, 100 RPM and 120 RPM, corresponding to tip speeds v_{tip} of 0.59 ms^{-1}, 0.82 ms^{-1}, 1.18 ms^{-1} and 1.41 ms^{-1} respectively. Tubes secured to the reactor's rear are connected to gas spargers at the reactor bottom. A macro and micro sparger configuration is available on the used sparger. The 150 holes on the micro sparger have a 0.15 mm diameter each. This study does not make use of the macro sparger. The gas rates used are 0 l min^{-1}. The deionised water used in the reactor is kept at a temperature of (20 $\pm$ 0.2) °C, which corresponds to a density of (998 $\pm$ 2)kgm^{-3}. An oscillating U-tube density metre (Anton Paar GmbH) is used to verify this.

Visual tracking setup

Visual tracking of the LSPs is done using a camera set up to track the LEDs in the LSPs. The video data thus obtained is then processed by the Particle tracking Velocimetry(PTV) code based on the code developed by Kamp [Kam22]. The camera used in the study is a Nikon D7500 with a 35 mm camera lens with f/5.6. The recorded video's frame rate is 24 frames per second, and the exposure time is 1/100 s and ISO 320.

The camera is mounted on a rail at a distance of 2.1 m from the reactor. The camera is set to have a clear view of the mirror setup adjacent to the reactor. The mirror is 1 m x 1 m in dimensions and is set at an angle of $\approx$ 50 ° from the reactor. The setup is shown in figure 3.13. Thus the single frame has two views of the reactor and creates a virtual second camera. This setup is inspired by the setup of Stewart et al. 2015 (Fig 3.14) but done on a larger scale [Ste15]. However, the data from the virtual camera is not used in the discussions of this study as the post-processing code for a 3D CTV could not be developed at the given time of the study.

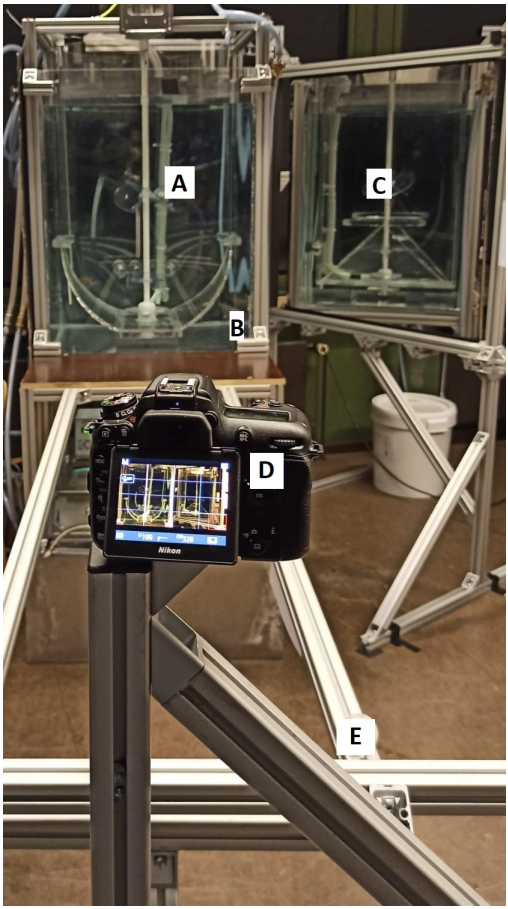

Figure 3.13.: Camera and Mirror setup for 200 L reactor with (A) reactor, (B) outer container, (C) mirror, (D) camera and (E) camera rail

The duration of each recording is set to 10 min, with three LSP equating to about 30 min of recording for each LSP. If one of the LSP stops working, the recording time is suitably increased to get 30 min of total recording time, consequently leading to an actual recording time of 10 to 30 min depending on the number of active LSP.

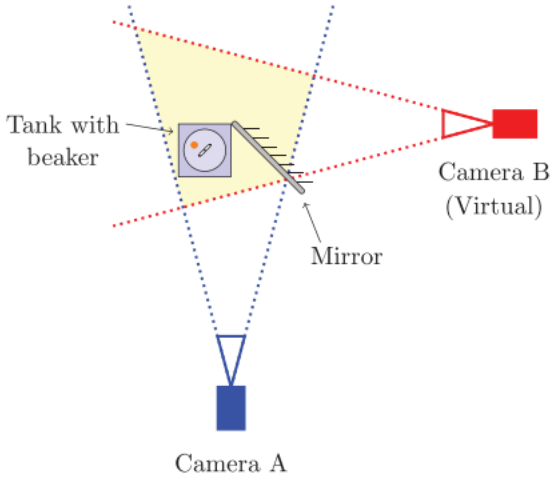

Figure 3.14.: Representation of the camera setup where the mirror acts as a virtual camera and the yellow shaded region represents the intersection of the field of views of the cameras [Ste15]

Calibration target

The loaded images are calibrated to correlate the images to actual distances in the reactor in the Matlab code. An aluminium frame supports a white PVC tarp covered with black dots in an equidistant grid as the calibration target. The target is 0.9 metres tall and 0.55

metres wide. The dots printed on the target are 20 mm apart and have a diameter of 5 mm centre-to-centre. The front and side images of the reactor with the calibration target are shown in Fig 3.15. The calibration targets are adjusted to fit the centre of the reactor in the front image.

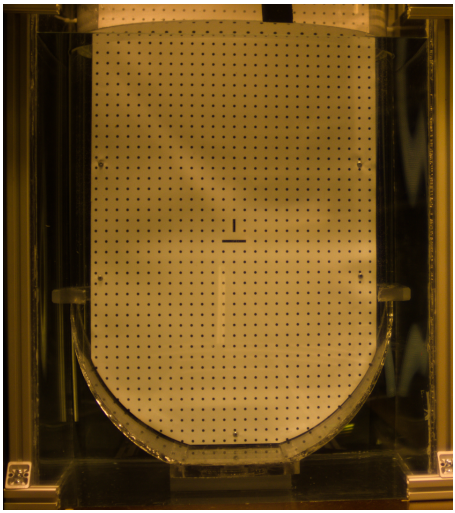

Figure 3.15.: The front images of the reactor with the calibration targets from the camera perspective

The target is put into the reactor before the experiment begins, with the printed side of the tarp facing the camera or the mirror for the front and side calibration, respectively. To establish a reference for MATLAB's reconstruction of real space coordinates from pixel coordinates, ambient light is used to record the reactor and calibration target. The camera and associated equipment will not be moved or shifted beyond that moment of measurement.

These calibration images are then used in the Matlab particle detection script developed by Kamp [Kam22] for the identification

and tracking of self-illuminated particles for the visual tracking of the flow behaviour of the particles, which is discussed in the next section.

3.2.2. Particle tracking Velocimetry

The script used for Particle tracking Velocimetry (PTV) is based on the one developed by Kamp, which in turn is based on the 2D-Particle Tracking Velocimetry algorithm developed by Nikki Indresh Lal (project work at the IMS (2019)). Kamp improved the visual recognition algorithm that can track Visuals not uniformly illuminated by LEDs, as with the LSPs in this study. This also incorporates the script to combine the locations of the particles into tracks and calculate the velocities and accelerations. The modified code can be found in Appendix H

The following steps are followed for the data processing in the PTV algorithm. Image preprocessing, LSP recognition, Calibration, distortion removal and translation into real space, particle tracking and finally, velocity and acceleration data calculation.

Image preprocessing

Image preprocessing is done to get the minimum image and has the following steps. Two consecutive images from the video are loaded into the MATLAB program, which converts them into image matrices. Then these matrices are compared to find the pixel with the lowest intensity. This is done separately for each of the primary colours. The end result is a video that has the minimum pixel intensity throughout the video. This minimum image is subtracted from the original video and converted into a grey-scale image based on the brightness cutoff set in the program. Thus only the parts in the image where the LED is detected are set as white (255), and the rest are set to black (0). then any pixel inside an area enclosed in white is also converted to white. Next, all white areas outside the reactor mask, the edge

defined manually by selecting points around the reactor border, are set to black.

LSP recognition

The LSPs are recognised by applying a MATLAB function to find circles of predefined size on the preprocessed images. The centre point coordinates of each circle in each image in order are saved into a matrix along with a number that represents the function's confidence that the circle is correctly detected. Any circle that falls below a modified certainty threshold is eliminated. Due to the LSPs' two LEDs, the image will have two distinct light areas. The matrix containing the coordinates of the circle centres is subjected to a separate procedure to identify clusters to achieve a single position per LED Mote. Additionally, every LSP location that is recognised for 48 frames (2 seconds of recording time) is consecutively removed from all subsequent frames to prevent erroneous results from LSP stuck in the reactor tubing.

Calibration

During the calibration, the image of the reactor with the calibration target inside is used. The same method used in the particle detection step is utilised to identify the printed dots. Any points incorrectly identified after automatic recognition are manually erased, and any missing points are added. The manual adjustment is made visually because the identified dots are shown over the examined image. All points are saved into an n-by-2 matrix after the last adjustment. Which is split into two n-by-1 matrices. The first corresponds to the X coordinate, and the second to the Y coordinate. The results are visually validated for inaccuracies by displaying the analysed image and individually colouring in the rows and columns after each dot has been assigned to exactly one row and one column. In the event that any of the dots are incorrectly assigned to a particular row or column, the calibration procedure is redone with new setup

parameters. The resulting rows and columns are stored in one array and another, respectively, if there are no problems.

Distortion removal and translation into real space

Then the pixels found in the LSP detection step are converted to real space coordinates by adjusting based on the calibration data. To do this, two target rows and two target columns with the closest average Y-position to each found point's Y-position and X-position to the point's X-position in the currently translated frame are identified and recorded separately for each found point in each frame. The nearest two points on each row and each column to the translated point are located and recorded in an array for each row and column. As a result, a location in actual space is assigned to each of the two dots per row or column. These assignments involve an interpolation that is carried out in stages. The position of the point in the real world is estimated for each of the two rows and columns separately in the first interpolation phase. An interpolation between the two dots in the upper row is done to determine the point's X-position. For the two dots in the lower row, this is repeated. The same is done for the Y coordinate. If the point is precisely on the corresponding row or column used for the calculation, these approximated locations would be the real space X- and Y-positions. The second interpolation phase involves calculating real space X- and Y-positions. An interpolation between the two computed X-positions determines the point's real space X-position. This interpolation is done based on the point's Y-position and the two average Y-positions of the rows from which the two X-positions are determined. Based on an interpolation between the two determined Y-positions, this procedure is repeated to determine the Y-position in actual space. Once a real-world position is determined for each point identified by the LED Mote detection process, the resulting final X- and Y-positions are saved, and the following point is translated.

Particle tracking

After finding the true positions of all LSP for every frame, the positions, the frame number for each position and the current length of the track is loaded into the track recognition script. Every point from the initial frame receives its individual track entry, which is then kept in an array. Beginning with the second frame, two new arrays are created to store the current X and Y positions and those from the previous frame. The velocity array stores the positional difference between the current and preceding frames. The array anticipating the positions of the next frame is saved as the sum of the positions of the current frame and the velocity array.

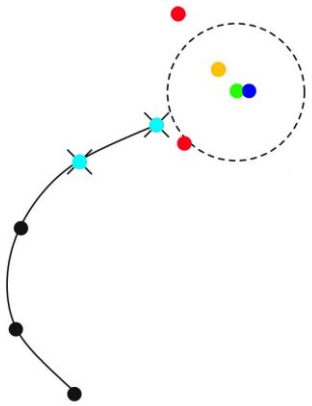

Figure 3.16.: The tracking algorithm's schematic. The threshold radius (dotted line), two prior track positions (turquoise), the anticipated next position (green), the best-fitting candidate (blue), the least-fitting candidate (orange), and spots outside the threshold radius (red) are all shown [Oue06].

The square of the differences between the estimated next X- and Y-coordinates for each track with a position added to it in the previous two frames is calculated, and the sum of the X- and Y-differences is saved to a new array entry for each point. Doing this, a measure for the distance between each track's predicted future track location and the current frame's positions is discovered. The resulting position is recorded as the following position for this track if just one of the generated distances is less than a manually chosen threshold. The position corresponding to the most minor difference between anticipated and actual positions is saved if numerous distances exceed the threshold. The schematic of the same is shown in Fig 3.16. The 3-Frame best estimate of the previous velocity can be used to describe this approach [Oue06, Kam22].

3.2.3. 15000 Liter Reactor and Setup

The second reactor tank used in this study is an acrylic glass tank that is similar to the stirred tank reactor developed by Boehringer Ingelheim Pharma GmbH & Co. KG with an inner diameter of 2 m and a volume V_r= 15 m^3. The reactor has a bottom-mounted magnetic agitator (ZETA BMRF) with 3 Elephant Ear (EE) impellers mounted on it, which have the impeller diameter(d_2) to reactor diameter (d_1) ratio $R_{d2d1} = \frac{d_2}{d_1} = 0.45$. An open tube sparger is located below the Pitched Blade impeller. This setup has no gassing and has impeller speeds of 15, 25 and 35 rpm translating to tip speeds of 0.7 ms^{-1}, 1.1 ms^{-1} and 1.6 ms^{-1} respectively. Thus the process parameters between the two reactors have been kept at approximately similar values. The difference between the two reactors is the presence of 4 baffles in the 15000 L reactor. The shape of the reactor is also different as it has a cylindrical body with a dish bottom. The width of the baffles is W_b=$d_1/10$, where d_1 is the diameter of the reactor. The shape, size and number of impellers are also different. Figure 3.17 shows a long exposure image of the LSPs in the 15000 L reactor.

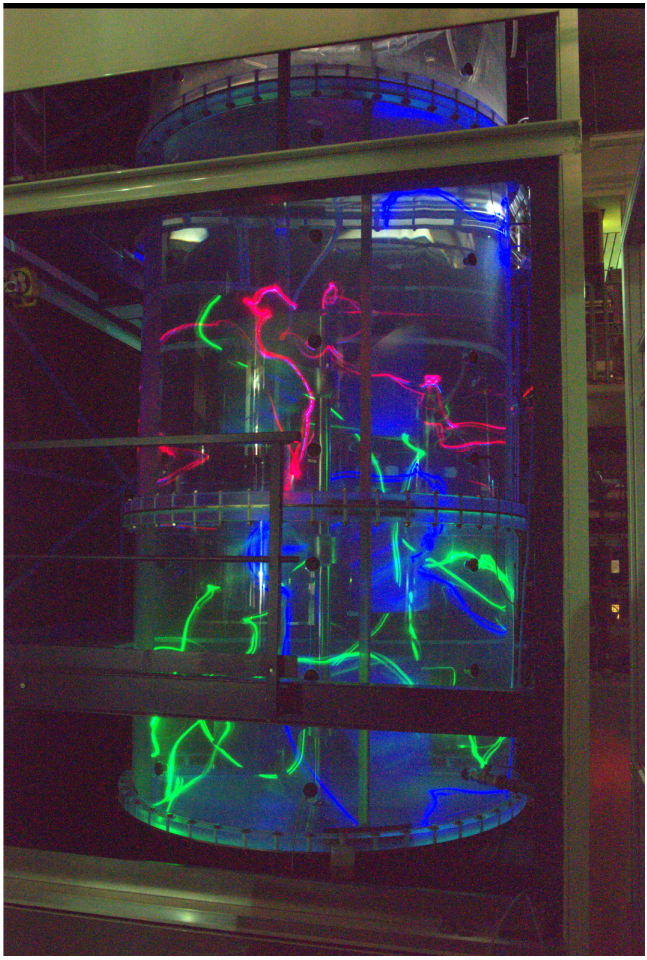

Figure 3.17.: Long exposure shot of the ISPs in 15000 L reactor with the red, blue and green trails of the respective LSPs in the reactor.

3.3. Validation of Sensors

Both the pressure and IMU sensors are first calibrated and validated individually. The pressure sensors are calibrated before the experiments to find the conversion factor for converting the measured pressure to the hydrostatic height. The sensors are validated after the trials to maintain the reliability of data from the sensors. This is also done to ensure the sensors function properly and are not damaged after or during the trials. A simple pendulum is used to calibrate the IMU. Although the IMU chip used has its internal calibration, this is done to ensure that this calibration matches the actual data. Although the IMUs do not come in contact with the liquid, there is still a chance for the same to incorporate some errors due to other factors like static or humidity. Thus they require validation after the trials. The validation and calibration of the IMU are done with the same experiment. The calibration and validation procedure and the results are discussed below.

3.3.1. Pressure Sensor Validation

The pressure sensor is fine-calibrated with a 50 cm water column and a pressure sensor mounted at the bottom of the column. Columns are filled with deionised water and the pressure changes with changing water column height. This is repeated 3 times. This pressure is then converted into hydrostatic height using a 0.971 conversion factor, which is more in line with the calibration data than 0.9801, which is the direct conversion from hPa to cm in hydrostatic pressure. $Depth = (P_r - P_{r0})/0.971$. Thus, the formula to calculate the height in cm at which the sensor is located in water. The calibration graph is shown in figure 3.18.

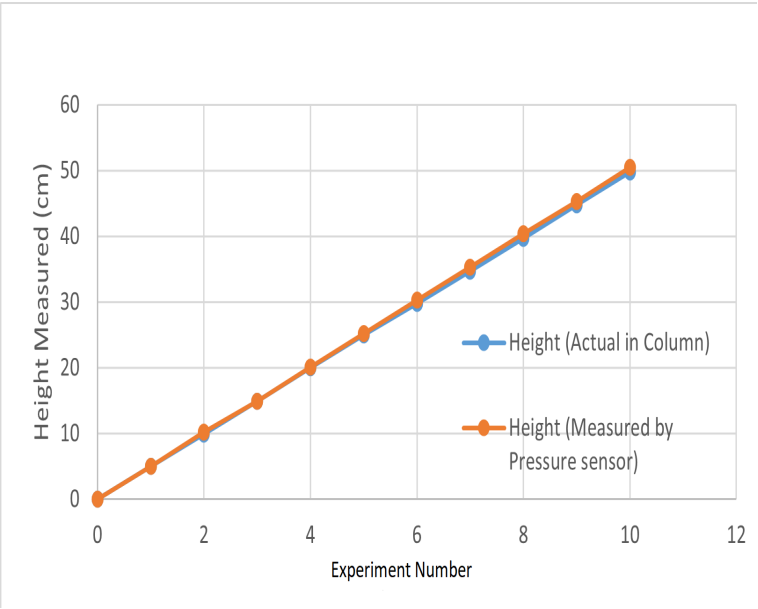

Figure 3.18.: Pressure sensor fine calibration over a water column

The pressure sensor is calibrated by a similar water column arrangement, where the pressure sensor is mounted at the bottom of a 5 m column. Although the sensor is rated for 1200 hPa, it is found that it can measure data up to 1500 hPa. When utilising the sensor to measure pressure levels that exceed the recommended range, it is crucial to verify the accuracy of the collected data post-experiment. This is necessary to confirm the stability of the sensors during and after the trials. The hydrostatic pressure is plotted against the recorded pressure from the sensor, and the fit is observed. The R is found to be greater than 0.99, Fig 3.19. This procedure was repeated before and after the experiments to ensure the data from the sensors was accurate.

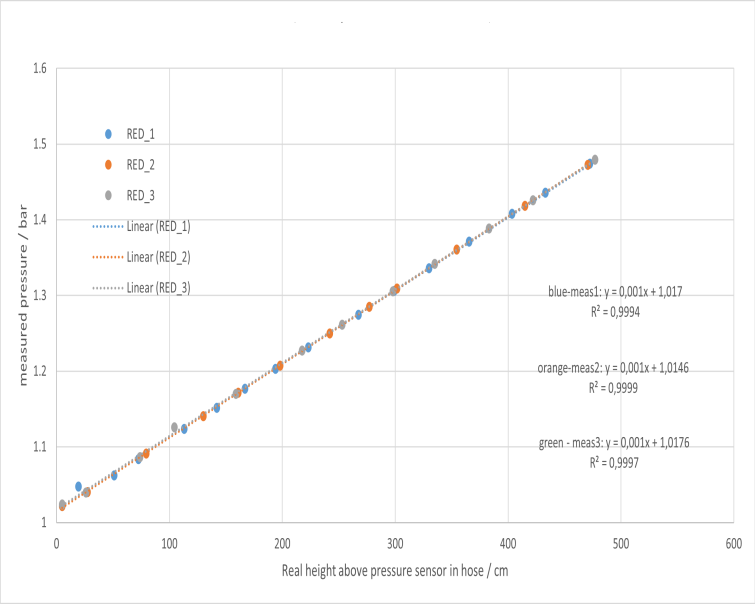

Figure 3.19.: Pressure sensor validation over a water column of 5m height

3.3.2. IMU Calibration

The IMU is calibrated by measuring the acceleration profile from the sensor with respect to the actual acceleration profile of a pendulum. The measured acceleration profile is compared to the acceleration obtained by the 2D Particle Tracking Velocimetry. The pendulum used for the experiment is set to be 2 m long from the top to the centre of the mote. The total mass of the pendulum is 499.8g. The initial angle of displacement is set to 5°. This setup allowed a relatively linear motion to the pendulum by restricting the vertical displacement. Fig 3.20 shows the pendulum setup used to calibrate IMU. The data from the IMU is compared to the data from Particle

Tracking Velocimetry. Then the filter values in the AHRS and filter algorithm are adjusted to match the value from the PTV data.

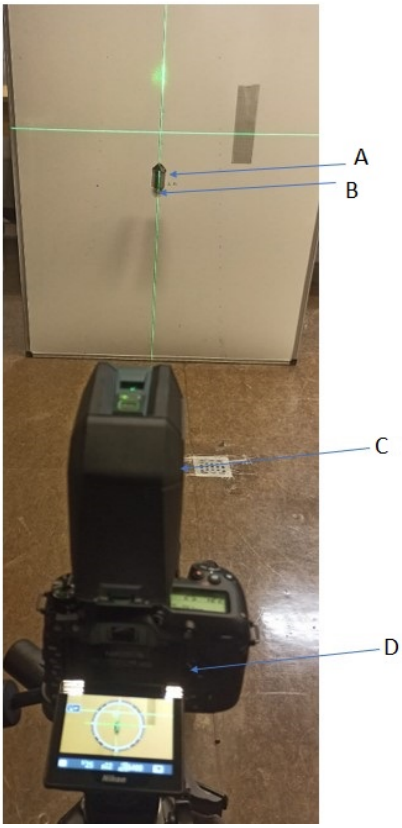

Figure 3.20.: IMU Validation setup with (A) pendulum mass, (B) IMU instrumentation attached to the bottom of the pendulum mass, (C) laser calibration device, (D) Camera

The figure 3.21 shows the correlation between measured and filtered acceleration magnitude obtained from the AHRS filter algorithm (chapter 3.5.1) for the planar axis and between the acceleration magnitude measured by 2 Dimensional Particle Tracking Velocimetry. The particle is tracked for 30 seconds by the camera, and that is compared to the data obtained from the IMU sensor.

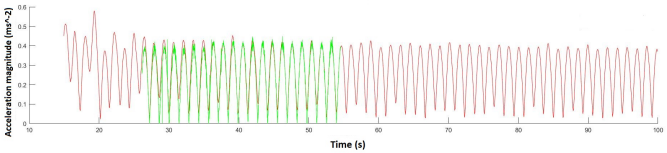

Figure 3.21.: IMU calibration Using Pendulum. Acceleration magnitude from IMU (red) plotted against Acceleration Magnitude obtained from 2D PTV (Green)

3.4. Experimental Procedure

The experiments in the study can be divided into three parts. The first part is the calibration of the sensors. The second part involves the adjustment of the LSP density. The third part is divided into two parts, where the experiments are subdivided into two different reactors.

3.4.1. Density Adjustment

In order to attain the desired density for the LSPs, we employ a solution made up of de-ionized water and sodium chloride sourced from PanReac AppliChem. This solution is separated into two containers with different mass ratios, resulting in two solutions with densities of 1000 kg m^{-3} and 1005 kg m^{-3} respectively, at a temperature of 20 °C. You can be confident that we control the density of the LSPs to comply with this specific range. Thus, maintaining a $\Delta\rho$ between

2 and 7. The fluid in the reactor is de-ionized water. The density of the particle is adjusted by changing the weight of the particle by adding ballast weights so that it sinks in the solution of 1000 kg m^{-3} and floats in the solution of 1005 kg m^{-3}. It is then sealed with a thin layer of silicone glue. The addition of silicon does not affect the density calibration. Since the dried silicon has approximately the same density as water. The sealed LSPs are retested for the buoyancy behaviour in the water bath.

3.4.2. Experimental Conditions and Procedure

The experiments are conducted in two phases for the two different reactors. The experiments for the 200 L reactor are given in Table 3.1. With impeller type of Rushton Turbine (RT) and Pitched Blade (PB) in two settings of RTPB and PBPB, four impeller speeds, no gassing, and two sensor types, a total of 16 experiments are conducted in the 200 L reactor.

Table 3.1.: Experimental settings for 200 L reactor

Impeller Types	Impeller Speeds(RPM)	Gassing rates(l min^{-1})	Sensor Types
RTPB	50		IMU
	70	0	
PBPB	100		Pressure
	120		

For the 15000 L reactor, the settings are stated in Table 3.2. There is only one impeller type with 3 Elephant Ear impellers, three impeller speeds, one gassing rate and two sensor types making a total of 12 experiments.

Table 3.2.: Experimental settings for 15000 L reactor

Impeller Types	Impeller Speeds(RPM)	Gassing rates(l min^{-1})	Sensor Types
PBPBPB	15 25 35	0	IMU Pressure

3.5. Data processing

This section discusses the algorithms used for processing the data received from the LSP. Two different algorithms are used, one for each LSP type.

3.5.1. IMU data processing

The IMU data needed processing by a MATLAB algorithm to adjust the data for correct attitude and heading (Appendix G. This is done using the Mahony AHRS algorithm discussed in chapter 2.3.2. Prior to the application of the AHRS algorithm, the attitude and heading are unknown for the LSP. Thus any change in angular direction would lead to a different heading. Therefore the data collected from the sensor is not representative of the actual data with respect to the reactor or the earth's gravitational field. The AHRS algorithm corrects the acceleration data and makes it relative to the Earth's gravitational and magnetic fields [Mah08]. Thus the X-axis of the data is always pointing to the magnetic north, and Z-axis is always pointing away from the ground (Fig 3.1.

The linear acceleration is derived from the corrected data, which is sent through a set of filters with preset filter cutoff values. Then the linear acceleration data is integrated to get the linear velocity data. This is again set through a set of filters. The MATLAB function *filtfilt* is used for the data filtering. The filter values are

realistically adjusted during the calibration step (Chapter 3.3.2. The steps involved in the data processing of the raw IMU data are shown in Earth's fig:3.21.

After obtaining the velocity and acceleration data, the relevant graphs for the PDF are plotted.

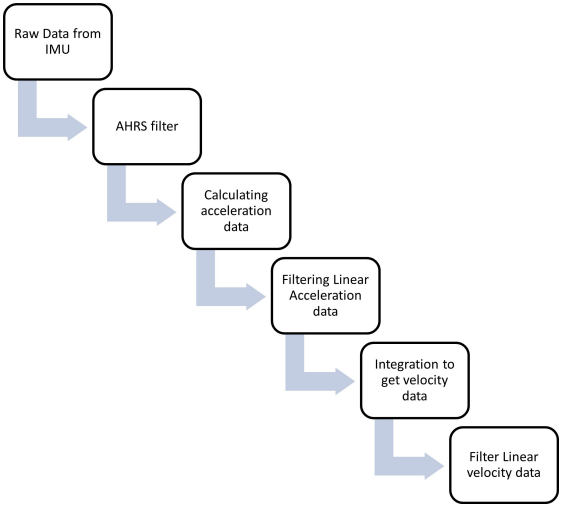

Figure 3.22.: The data processing steps used for IMU data.

3.5.2. Pressure data processing

The data received from the Pressure LSP is first cut to get appropriate experimental data. This data is converted to an *.xlxs* format, and the pressure is converted to depth. This data is loaded into the MATLAB program that converts the depth data to height and then differentiates that to calculate the axial velocity data and then the PDF of the same. Then the data is plotted for easier understanding.

4. Results and Discussions

This chapter contains the experimental results that were conducted regarding the Lagrangian Sensor Particles (LSPs). The Chapter is divided into three sections. The first section has the results from the 200 L reactor with the data from the Pressure LSP, the IMU LSP and the Particle Tracking Velocimetry. The next section has the results from the 15000 L reactor that consists of the data from the two LSP types. The final section discusses the various errors that may have affected the results of the experiments.

4.1. 200 L Reactor

The following are the results obtained from the trials done in the 200-litre reactor. These include the data from the IMU, Pressure sensor and Particle tracking velocimetry results. The first part shows the results from the PTV. The second part compares the results from the Pressure sensor and the PTV results. Next, the results from the IMU sensor and the PTV were compared. Finally, the results from the pressure and IMU units were compared.

4.1.1. Particle Tracking Velocimetry results

The Probability distributions determined by the Particle Tracking Velocimetry (PTV) are plotted across the face of the reactor grid. The grid is divided into horizontal sections of 60 mm (d/10), which is 1.5*d_P, making it easier for detection with considering the curvature of the reactor. Thus the grid used in this experiment has the same width as the one used by Kamp, but the height of the grid cells is

the radius of the LSP [Kam22]. The vertical sections are 20 mm, which is the radius of the LSP. The instrumentation in the LSP separates the LEDs in the LSP. Thus there are points where only one LED is visible from the viewing angle of the camera. The LEDs are assumed to be 1 cm from the centre point of the LSPs in the program. Sometimes the LEDs are hidden due to various obstacles in the tank, and also, there are certain conditions in the PTV code that discards data if it does not meet the criteria. Thus only about 1/3 of the expected data is taken into account for the actual evaluation.

Figure 4.1 shows the PDF distribution heat map comparison between IMU LSPs and Pressure LSPs moving in a 200 L reactor with two PB impellers. The PDF show a similar distribution for similar cases. The plot shows that at the impeller's low velocity (50 RPM), the LSPs are mostly distributed at the bottom half of the reactor. At higher velocities like 120 RPM, they are much more evenly distributed across the reactor. Figure 4.1 also shows that both the LSP types have a similar distribution profile across the reactor. From this, we can safely assume that the IMU LSPs and the Pressure LSPs have similar flow properties due to them being the same size and in the same density range of 1001 and 1005 kg/m^3.

The other observation that can be made from fig 4.1 is that the tracks of the LSPs closer to the walls of the vessel are very low. This may be due to the code removing the data points that appear closer to the walls. This is due to the reflective nature of the vessel and the condition in the code to ignore any brightness above or below a certain threshold. This is to avoid the parallax error caused due to the cylindrical shape of the reactor. Also, it can be seen that most of the movement of the LSPs is close to the impellers in the reactor, and at slower speeds, it is mostly around the bottom impeller. The bottom impeller's centre is 0.15 m from the bottom of the reactor, and the top impeller's centre is 0.45 m from the bottom. Both impellers are 0.2 m in height.

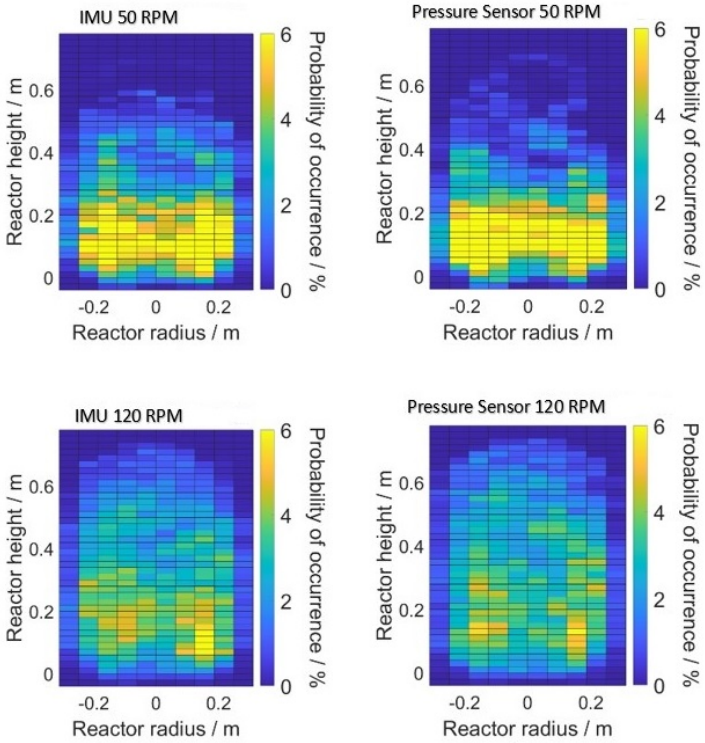

Figure 4.1.: Probability Density Distribution for Pressure and IMU LSPs with PBPB impeller setup and no gassing. The colour of each region represents the likelihood (as a percentage) for an LED LSP to occur within the respective interrogation window.

4.1.2. Pressure vs 2D-Particle Tracking Velocimetry

In this section, the data from the Pressure LSPs and the 2D-PTV are compared. Figures 4.2 show the axial Probability Distribution Function(PDF) over the normalised height of the reactor from the data of both the pressure LSP (right) and the PTVs(left). The normalized height of the reactor is used so that their results are comparable to the results from the 1500 L reactor. The highest axial velocities are near the lower impeller, which is between 0.2 m and 0.1 m from the bottom of the reactor.

As seen from the figure, the probability distribution over the reactor's normalised height is very similar in both cases. As discussed in the earlier subsection, the axial distribution is directly linked to the speed of the impeller and is affected by the lack of baffles in the reactor. Due to the absence of baffles in the 200 L reactor, most of the motion occurs in the radial direction and not in the axial direction. This phenomenon is even more visible in the PBRT impeller setup shown in figure 4.3, where the Rushton Turbine impeller situated at the bottom of the setup has a more radial flow. This is unable to lift the LSPs when they reach the bottom of the reactor.

In some cases with low impeller velocity, for example, in figure 4.3, at 50 RPM, the LSPs are sometimes stuck at the bottom of the reactor, and this is observed in the Pressure LSP data but not in the PTV data due to two factors. The first cause is tubes for gassing which are situated behind the impeller rod. The LSPs get stuck on these and thus are not visible on the camera. The second reason is that the PTV code does not consider any LSPs that have not been in motion for more than 2 seconds or 24 frames of the video.

Figure 4.4 and figure 4.5 show the comparison of the mean axial velocity over the normalised height of the reactor for both Pressure LSP and the PTV data for PBPB and PBRT setups, respectively. The axial velocity measured by the pressure sensor shows a consistent increase in the axial velocity with an increase in the impeller speed. Also, compared to the two impeller setups, the PBPB setup has an evenly distributed velocity profile across the height of the reactor. In

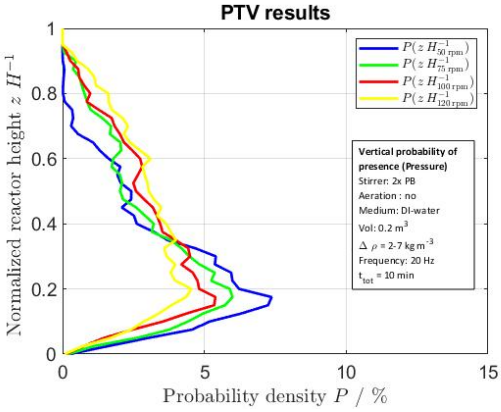

(a)

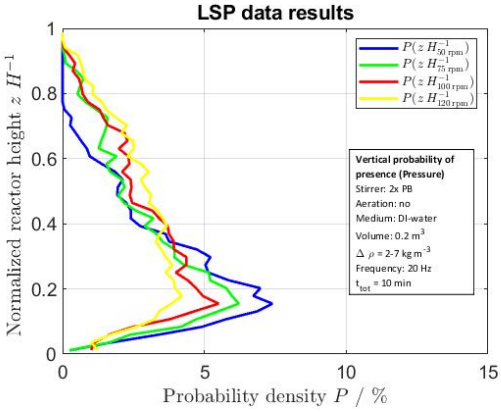

(b)

Figure 4.2.: Comparison between the PDF of the sensor along the height of the reactor as observed by Particle tracking using PTV (a) and Pressure LSP (b) for PBPB impeller setup

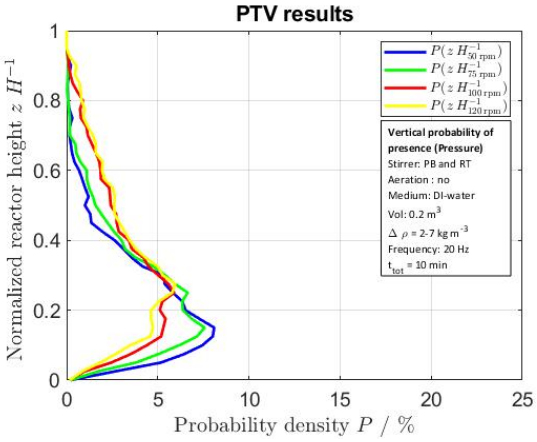

(a)

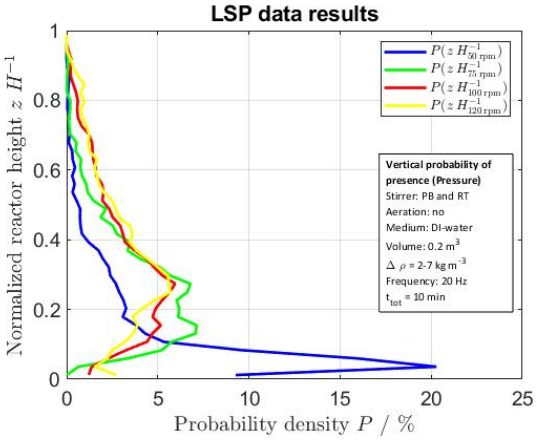

(b)

Figure 4.3.: Comparison between the PDF of the sensor along the height of the reactor as observed by Particle tracking using PTV (a) and Pressure LSP(b) for PBRT impeller setup

contrast, the PBRT setup has higher velocities at the bottom half of the reactor. This has two probable causes, first is the shape of the reactor that causes higher radial motion, and the second is the radial fluid motion caused by the impeller pushing the LSPs towards the curvature of the vessel walls and the absence of baffle to prevent this radial motion.

The axial velocity data obtained from the PTV seems inconclusive at first glance. This may be due to the very high axial velocities reported by the PTV at the top and bottom of the reactor. This is caused due to the PTV code discarding all data from the bottom of the reactor that does not meet the criteria of being in motion for more than two seconds and also the fact that the sparger in the reactor hides the LSPs. At the top of the reactor, there is very little motion at low speeds as the LSPs are mostly bound to the bottom of the reactor at low speeds. The rejection of about 65 percent of the data and inconsistent data at the top and bottom of the reactor skews the PDF results of the PTV. Also, the LSPs are sometimes hidden by the impeller or impeller rod and paraphernalia. The velocities appear higher at the very top and bottom because only one directional motion is captured at these zones. As mentioned earlier, only the LSPs that have been in motion for more than 2 seconds are considered. This leads to skewed results in these zones.

Thus the trends from the PDF of the axial velocity of both data sets cannot be properly compared over the normalised height of the reactor. Although, higher impeller speeds lead to higher axial velocities. The distribution of velocities is more even for the PBPB impeller setup, and the axial velocities in the bottom half of the PBRT impeller setup are generally higher by a factor of around 1.3 to 1.5.

4.1.3. IMU vs Visual results

This subsection compares the data from the IMU LSPs and the PTV. Figures 4.6 and 4.7 compare the PDF of the acceleration magnitude determined by the IMU and Visual methods for PBPB and PBRT

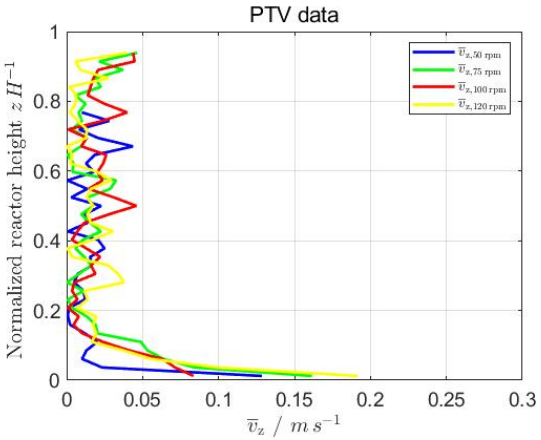

(a)

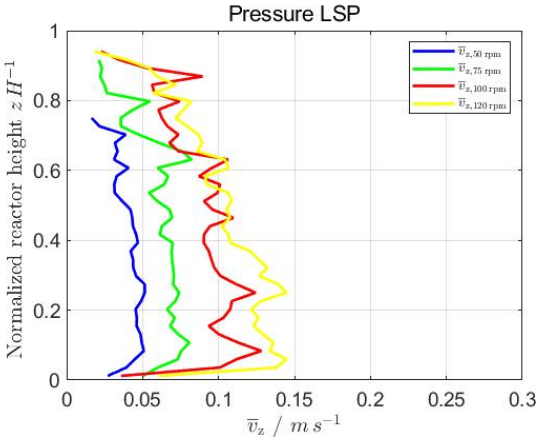

(b)

Figure 4.4.: Comparison between the axial velocity distribution along the normalised height(z/H) of the reactor as observed by PTV (a) and Pressure LSP(b) for PBPB impeller setup

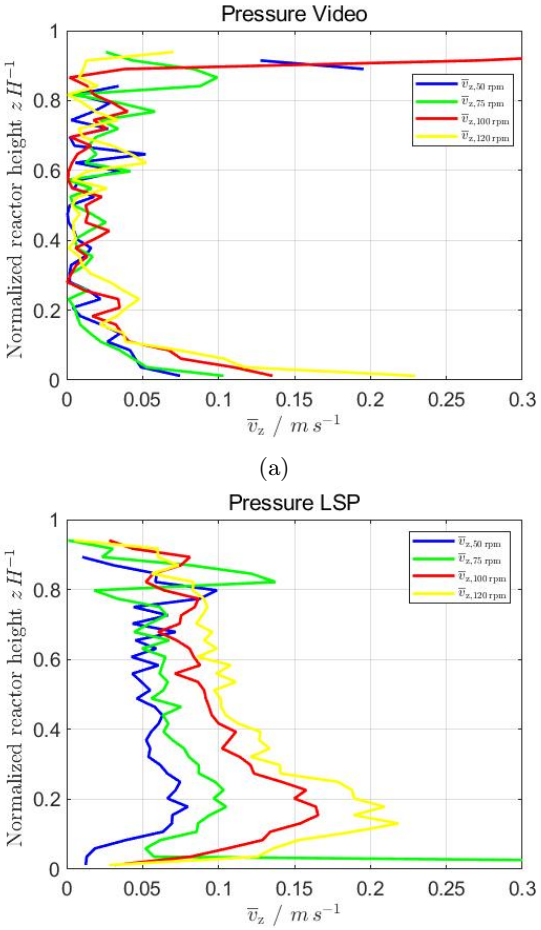

(a)

(b)

Figure 4.5.: Comparison between the axial velocity distribution along the normalised height (z/H) of the reactor as observed by PTV (a) and Pressure LSP (b) for PBRT impeller setup

impeller setups, respectively. The acceleration magnitude measured is on the front plane of the reactor, which is perpendicular to the ground and facing the camera. There is also a provision in the code to align the data from the IMU to the plane under observation by the camera using the magnetometer. The general trend of the PDF acceleration magnitude in the plane is that the acceleration magnitude is higher at higher impeller speeds. The planar acceleration magnitude is higher in the PBRT setup when compared to the PBPB impeller setup. This is due to the higher radial movement generated by the Rushton Turbine.

The Acceleration magnitude appears higher in the visual data as compared to the IMU data. This can be explained by the limitation of the video's inability to capture the movement in the axis parallel to the camera and the circular motion of the LSPs. Another factor contributing to the higher acceleration magnitude is the distortion caused by the curve in the reactor. This is further exacerbated by the fact that the raw data obtained by the video method is the positional data of each LSP and must be differentiated twice to obtain the acceleration data. Meanwhile, the IMU measures the acceleration data directly. Due to these factors, the camera perceives the LSP to be accelerating faster than it is in reality.

The velocity magnitude PDF for the data obtained by the visual methods and the IMU LSP is shown in Figure 4.8 and 4.9. These are for PBPB and PBRT impeller setups, respectively. These figures show that the velocity magnitudes measured by the IMU LSP and the PTV have a very similar distribution. The velocities measured by the IMU are still less than the same measured by the optical tracking. This is caused by the same reasons that affect the acceleration magnitudes in the previous figures. The only difference is that the velocity magnitude obtained by the IMU here has an integration drift. Therefore the reported velocities are slightly higher than the actual. This offsets the error caused by the previously listed reasons in the PTV, which appears to be almost similar or the same.

From the above comparisons, we can infer that the data obtained from the two LSPs are comparable and generated under the same

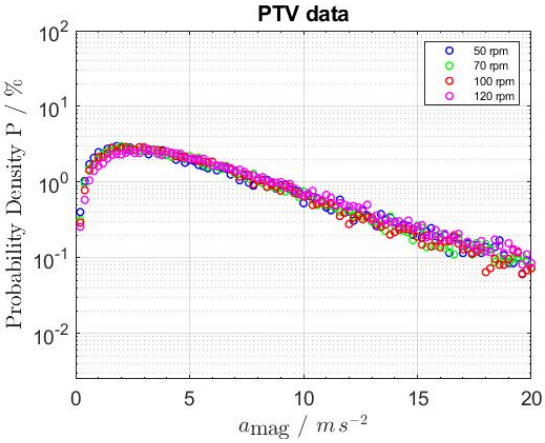

(a)

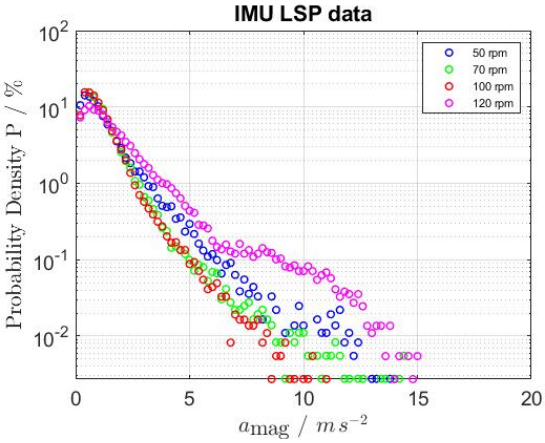

(b)

Figure 4.6.: Comparison between the PDF of Acceleration along the XY plane of the reactor as observed by PTV (a) and IMU LSP (b) for PBPB impeller setup

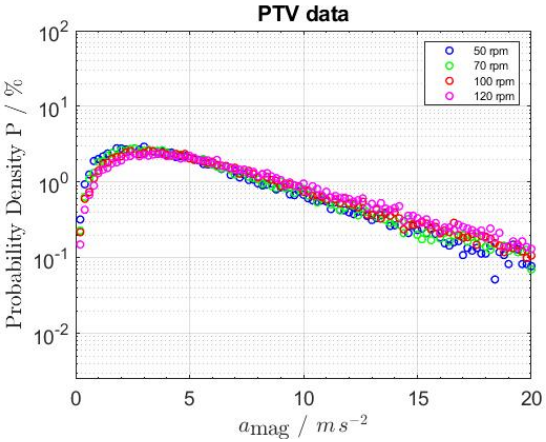

(a)

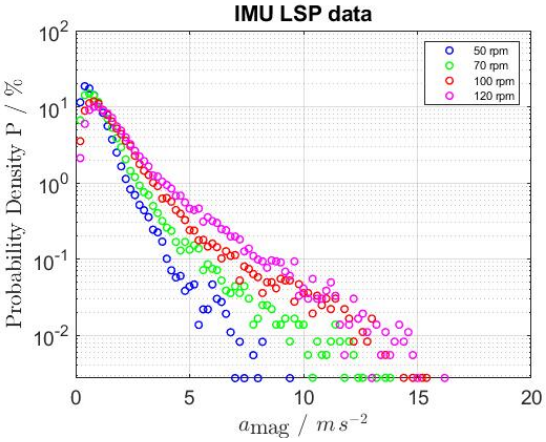

(b)

Figure 4.7.: Comparison between the PDF of Acceleration along the XY plane of the reactor as observed by Particle tracking using Video (right) and IMU LSP (left) for PBRT impeller setup

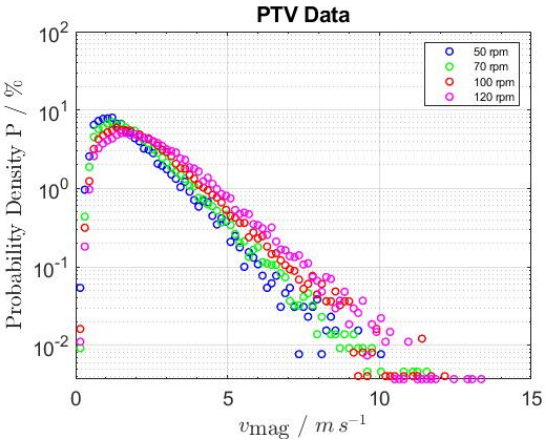

(a)

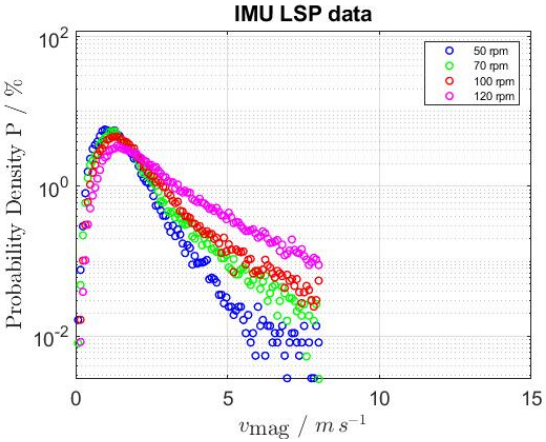

(b)

Figure 4.8.: Comparison between the PDF of Velocity in the XY plane of the reactor as observed by PTV (a) and IMU LSP (b) for PBPB impeller setup

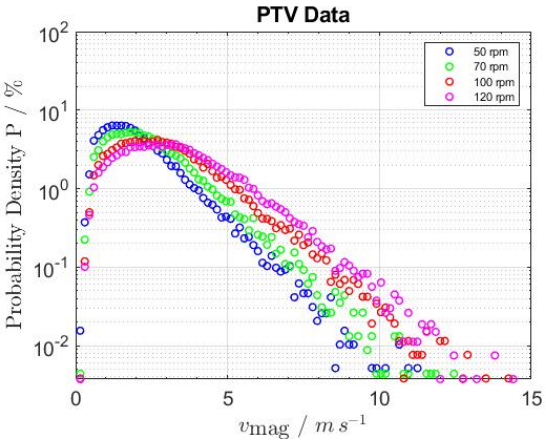

(a)

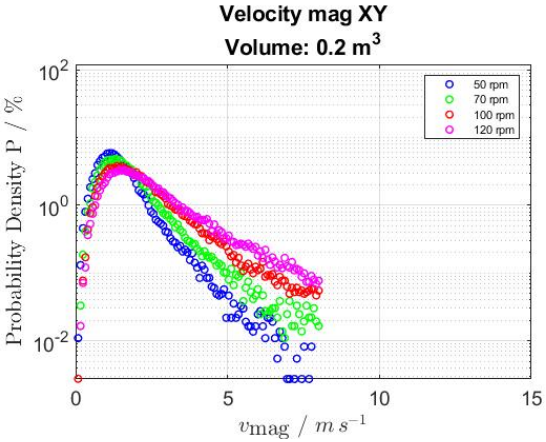

(b)

Figure 4.9.: Comparison between the PDF of Velocity in the XY plane of the reactor as observed by PTV (a) and IMU LSP (b) for PBRT impeller setup

conditions. They also confirm that the data obtained from the two LSPs are valid ad represent real data that was obtained from the PTV. Thus, in the next subsection, we can safely compare the IMU LSP and the Pressure LSP data.

4.1.4. IMU vs Pressure results

In this section, the data from the two LSPs are compared. Figure 4.10 and 4.11 shows the PDF of the axial velocities for PBPB and PBRT impeller setups, respectively, for four impeller speeds and under no gassing conditions. The graphs show a similar trend of moving towards higher axial velocities at higher impeller speeds. However, the Axial velocities measured by the IMU LSPs are seen to be a bit higher than the axial velocities measured by the Pressure LSPs by a factor of around 2.5 to 3. This may be due to reasons such as the measuring frequency and accuracy of the pressure sensor being lower than that of the IMU sensor. Another reason is that there is an integral shift in the data from the IMU as it has to be first processed to be aligned to the earth's axis, filtered, and then integrated to get the velocity data. Nevertheless, both sensors' PDF velocity magnitude profiles are similar and comparable.

Thus the sensors have been tested in the smaller reactor and successfully validated using the PTV. Therefore the LSPs can be tested in the larger reactor. The results are shown in the next section, the data from the LSPs tested in a 15 m^3 reactor.

4.2. 15000 L Reactor

This section shows the results of the data from the LSPs as they were tested in a 15 m^3 reactor at three different stirrer speeds of 15rpm, 25 rpm and 35rpm for a PBPBPB impeller. The results from IMU LSPs are shown first, followed by the Pressure LSPs, and finally, the data from both LSP types are compared to each other.

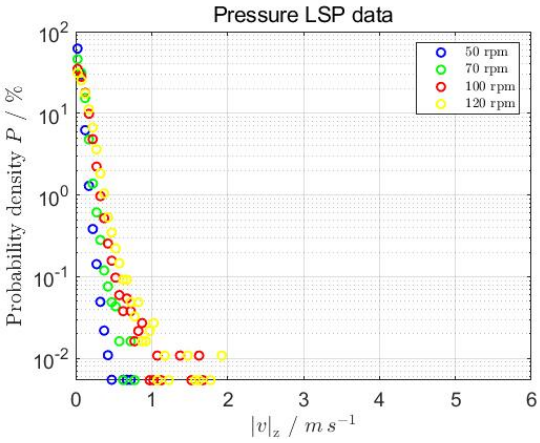

(a)

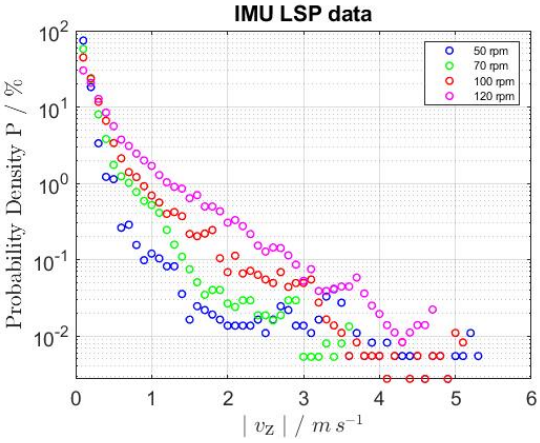

(b)

Figure 4.10.: Comparison between the PDF of Axial Velocity as observed by Pressure LSP (a) and IMU LSP (b) for PBPB impeller setup

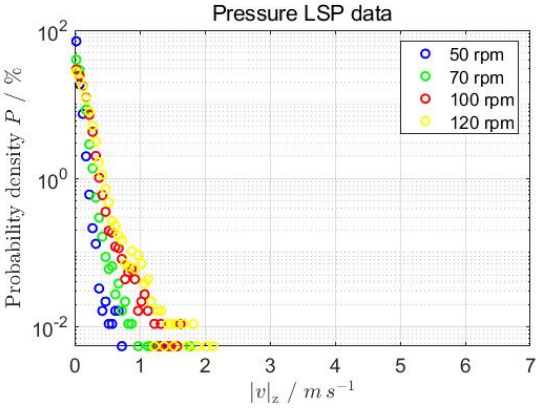

(a)

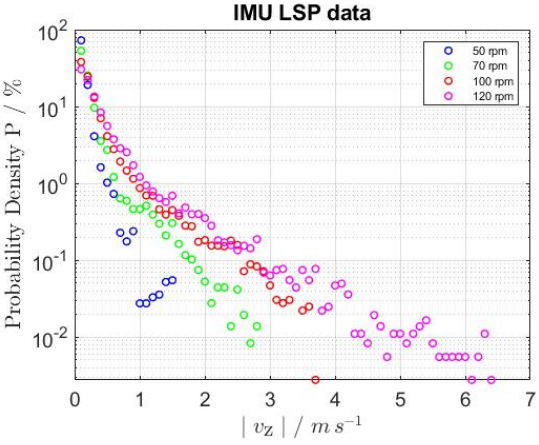

(b)

Figure 4.11.: Comparison between the PDF of Axial Velocity as observed by Pressure LSP (a) and IMU LSP (b) for PBRT impeller setup

4.2.1. IMU sensor results

This section shows the IMU LSPs results for the 15000 L reactor with PBPBPB impeller setup. Figure 4.12 shows the PDF of the acceleration magnitude of the LSPs in the reactor at impeller speeds of 15, 25 and 35 rpm. The data is consistent with the data from the 200 L reactor. The acceleration magnitude increases with the increase in the impeller speed. The maximum acceleration magnitude is in the range of 5 to 15 ms^{-2}

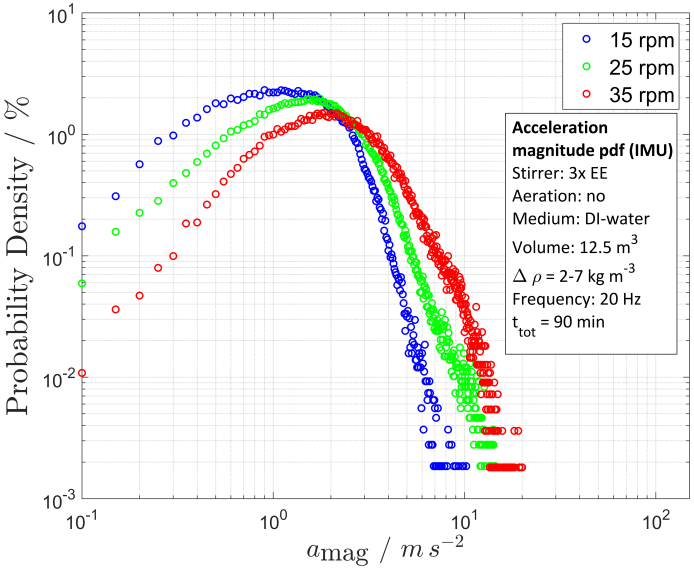

Figure 4.12.: PDF of the Acceleration Magnitude from the IMU LSP data for 15000 L reactor with PBPBPB impeller setup

Figure 4.13 shows the probability distribution of the velocity magnitude derived from the IMU LSP data in the 15000 L reactor with the PBPBPB impeller setup for the impeller speeds of 15,25 and 35

rpm. The velocity magnitudes observed have the highest distribution peak, slightly less than the respective impeller tip speed. Nonetheless, the maximum velocity magnitudes observed are much higher and range between 3 to 8 ms^{-1}. These velocity magnitudes may be slightly less than the actual magnitudes due to the errors mentioned in the previous sections.

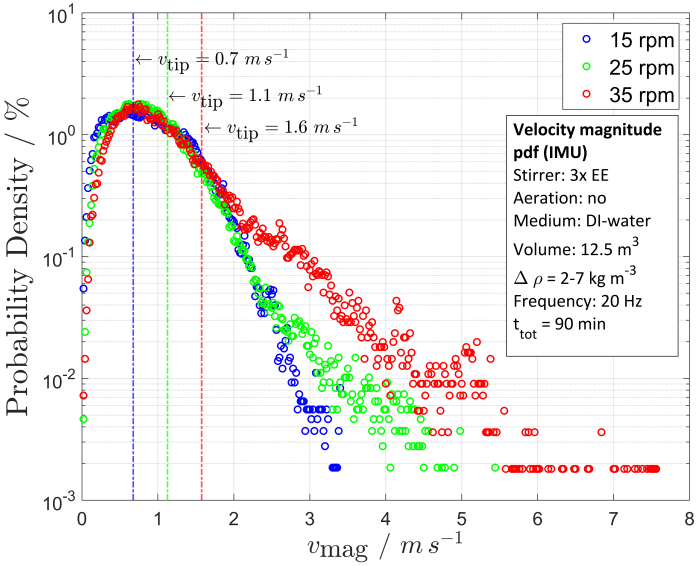

Figure 4.13.: PDF of the Velocity Magnitude from the IMU LSP data for 15 m^3 reactor with PBPBPB impeller setup

4.2.2. Pressure Sensor results

This section discusses the data from the pressure LSP for the trials in the 15 m^3 reactor with PBPBPB impeller setup. Figure 4.14

shows the probability distribution of the LSPs over the normalised reactor height. The distribution shows the tendency of the LSPs to be more evenly distributed at higher impeller speeds. It shows a higher tendency to be at the bottom of the reactor at low impeller speeds.

Figure 4.15 shows the mean velocity of the LSPs over the normalised height of the reactor. It can be observed here that the axial velocity at the top and bottom regions of the reactors are low and increase with increasing impeller speeds on the rest of the reactor. This is caused by the reactor geometry and the presence of baffles in the reactor, which lead to a more axial flow in the reactor, and the radial flow happens only at the top and bottom section of the reactor, where the axial velocities are minimum. This phenomenon is visually observable in the transparent reactor in which the trials were conducted and is validated by the data from the LSPs.

4.2.3. Data Comparison

This subsection compares the data from the IMU LSPs and the Pressure LSPs for the Trials conducted under similar conditions in the 15 m^3 reactor with PBPBPB impeller setup at the impeller speeds of 15, 25 and 35 rpm. From figure 4.16, which compares the axial velocity distribution measured and calculated from the pressure and IMU LSPs in the aforementioned trial conditions, it is observable that the axial velocity distribution tends to follow a similar pattern in the 15 m^3 reactor as in the 200 L reactor and the axial velocity measured by the IMU is higher than the axial velocity measured by the pressure LSP by a factor of 2 to 2.5 and this is caused by the same reasons that are discussed in the previous section. It is also observable that the highest probability of the mean velocity lies between 0.2 to 1.1 ms^{-1} for the data from the pressure sensor and between 0.5 and 2.3 for the data from the IMU LSP.

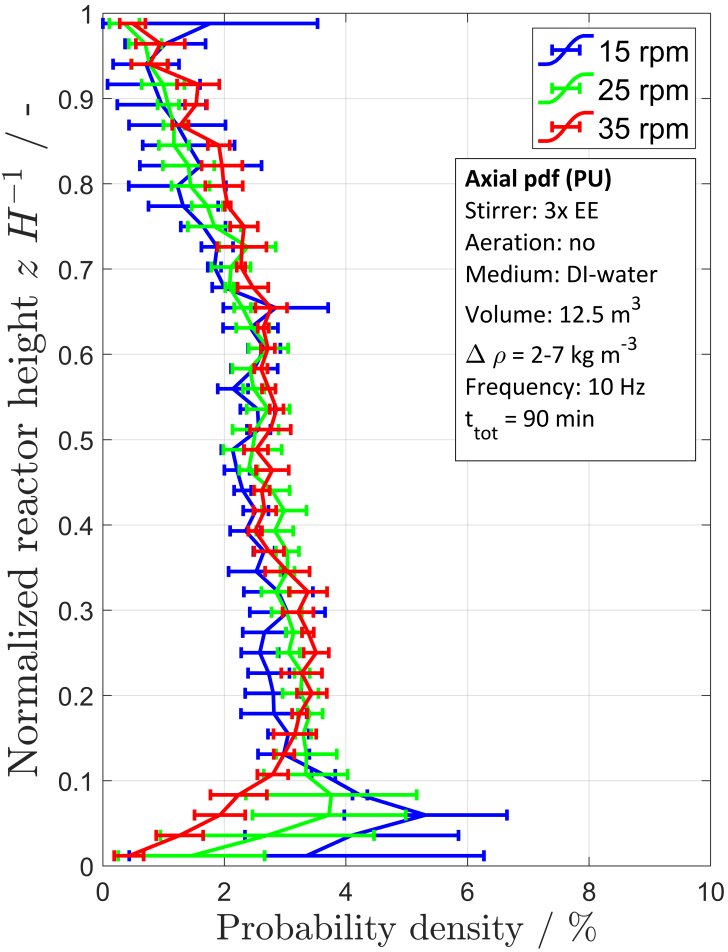

Figure 4.14.: Probability distribution of the Pressure LSPs over the normalised height of the reactor with PBPBPB impeller setup

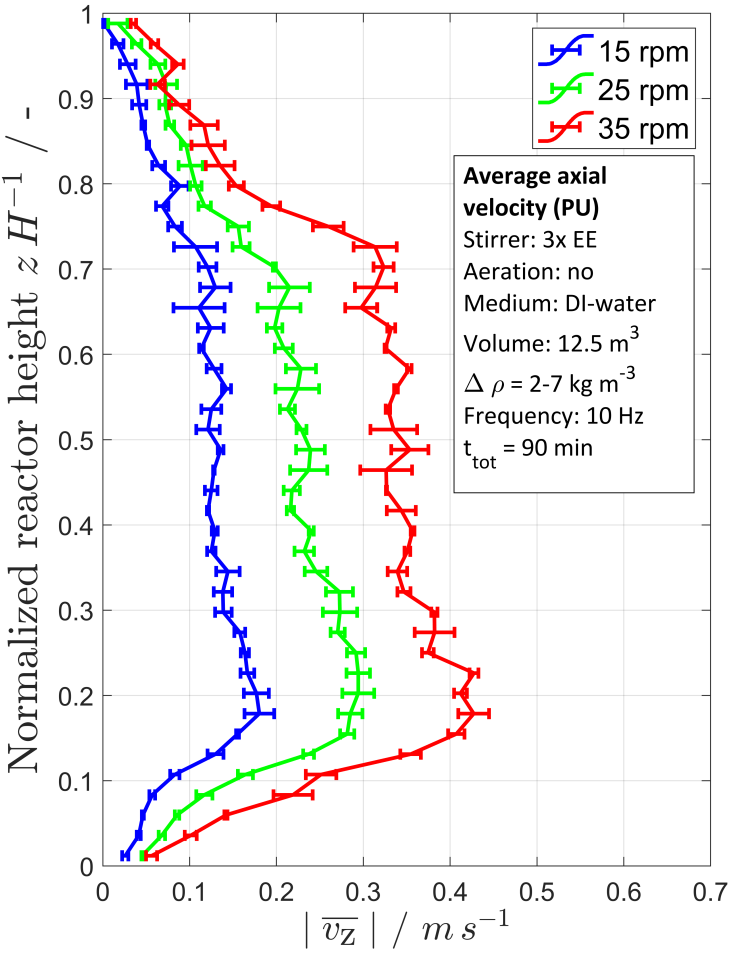

Figure 4.15.: Mean velocity vs the normalised height of the reactor measured by the Pressure LSPs in the 15000 L reactor

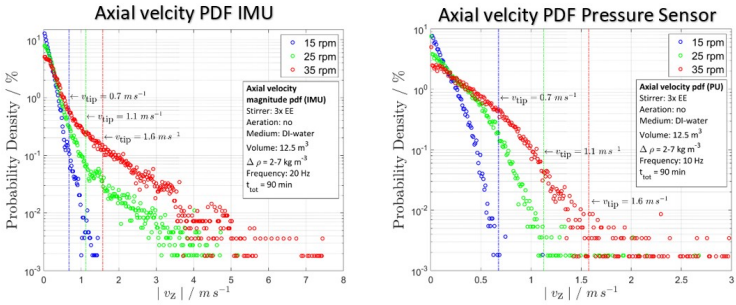

Figure 4.16.: Comparison between the PDF of mean axial velocity as observed by IMU LSP (left) and Pressure LSP (right) for 15 m^3 reactor

4.3. Error discussions

This section focuses on the various errors that may affect the final results derived from the raw data. These errors can be introduced from multiple parts of the experimental setup.

4.3.1. Error sources in Particle Tracking Velocimetry

For the PTV results, the errors coming from the reactor design and materials, the recording process, the camera setup and the parallax error, which is when the angle of observation is not parallel to the plane being observed in the camera's line of sight. Also, errors are introduced from the steps during the data processing.

Error sources in Experimental Setup

The camera is at a finite distance from the reactor (2.2m); thus, there are some distortions in the projection of the 3D space inside the reactor. This will cause the image of the LSP to move downward

when moving away from the camera and vice versa in the section of the reactor above the camera and move upwards when moving away from the camera and vice versa when below the camera. The impeller shaft and the aeration apparatus at the bottom of the reactor are not transparent and can hinder the detection of LSP behind them. This causes broken tracks, which lead to errors in the velocity data calculations. There are also some distortions caused by the reflection of the LED on the walls and the impeller blades of the 200 L reactor. Measures were taken in the script to reduce such errors by adjusting the threshold for the brightness of the mote that can be detected and adjusting the threshold of the minimum lengths of tracks to be recognised as valid data.

Error sources in PTV script

The MATLAB script developed by Kamp [Kam22] that was used to process the PTV data also has some points where an error may be introduced into the data. This includes the calibration being done only with respect to the centre of the reactor, as the calibration target is fixed to the diameter plane of the reactor and does not consider the reactor's curvature. Thus, any distortions due to refraction and parallax error while moving towards or away from the camera are not considered. The script also does not consider any tracks that are less than five frames or if the LSP has not been in motion for more than 24 frames. This leads to the discarding of a significant amount of data. It is as high as 65 per cent of the total data in some cases. This leads to a lot of misleading data where the probability distribution data is incorrect due to the exclusion of data where the LSPs cannot move due to insufficient lift in the reactor. Another possible error introduced by the script is the possible cross-linking of two LSP trajectories, causing a sudden shift in the velocity data. This happens when two LSP pass near each other, and there is a possibility that the code registers a sudden change in the direction of the LSPs. However, this is only a minor cause of error. However, these errors are reduced by extending the recording time of the trial

so that the uncertainties can be minimised.

4.3.2. Error sources in LSPs

Error sources in Pressure Sensors

There are also various error factors in the data collected by the LSPs. For the pressure sensors, the errors come from the delay between the change of the pressure and the time required by the sensor to register the same, which is affected by the length of the hose connecting the sensor and the outside. Also, there is a delay in recording the same data on the SD card, which may range from 1 ms to 5 ms per reading. There are also errors introduced due to changes in the atmospheric pressure, as the initial pressure of the atmosphere used to calculate the delta P does not remain the same throughout the experiment. This is followed by the errors introduced while the data is processed and during the derivation of velocity from the axial position data.

Error sources in IMU Sensors

The errors in the data from IMU come from sources like the lag in recording the data from the IMU to the SD card and the sensor going out of calibration due to outside interference, like the magnetometer being affected by the metal and magnetic parts in the reactor and stirrer system, causing a cascade of errors during data processing. There are also errors from the sudden shaking and spinning of the LSP caused by the collision of the LSP with the impeller blades or walls of the reactor. There are errors caused by the data processing when the filters are used or while using the AHRS algorithm to get the reoriented data [Bun20]. There are also errors caused due to integration shifts to get the velocity values from the acceleration values.

The study has been designed to reduce these errors as much as possible by calibrating the imaging equipment, the pressure and IMU sensors. Then the data from each method is compared to each other to ensure the data's validity.

5. Conclusions and Outlook

Two separate LSPs are designed with IMU, pressure sensors and other components that can be bought easily off the shelf. The circuitry is designed, and the sensor units are assembled and tested. The housing is developed in-house, and PMMA material is used to produce the same. These Lagrangian Sensor Particles (LSPs) are then tested in a 200 L reactor with two impeller setups and a 15000 L reactor with one impeller setup. The sensors are calibrated and validated, and MATLAB scripts are used to process the data from all three tracking methods.

The trials concluded with results about the probability distribution of acceleration magnitude, velocity magnitude and the Mean axial velocity of the LSPs. The axial velocity and the probability distribution of the LSPs over the normalised length of the reactor are also shown. Finally, the probability distribution of the axial velocity obtained from the pressure sensor and the IMU is compared.

Finally, the same trials are conducted in the 15000 L reactor, but only the LSP is used. The amount of data that could be collected in the 15000 L reactor through the visual method is limited by the size of the impellers and the inability to calibrate the entirety of the reactor for visual tracking. The data from the pressure and the IMU LSPs from the 15000 L reactor are analysed, and the acceleration magnitude and velocity magnitude from the IMU and the distribution of the LSPs across the normalised height of the reactor are evaluated individually. The mean axial velocity from the pressure sensor and the IMU are compared and found to be in accordance with the results obtained from the 200 L reactor.

The results are obtained, and the following conclusions can be safely made with a high degree of confidence. The acceleration and,

subsequently, the velocity magnitude of the LSPs in the reactor depend mainly on the impeller's speed. The secondary factor that influences the movement of the LSPs in the vessel is the presence of baffles in the reactor; other factors that affect the LSPs' movement are the reactor's shape and geometry. There is a direct correlation between the speed of the impeller and the rate of movement and acceleration of the LSPs in the reactor. Although the velocity of the LSPs may sometimes exceed the tip speed of the impeller, the probability and frequency of this occurrence are very small. On average, the velocity of the LSPs is about 0.5 to 0.9 times the tip velocity.

The above-stated factors similarly influence the probability distribution over the normalised height of the reactor. But the presence or absence of the baffles plays a significant role in this. The LSPs show more axial movement in the presence of baffles and a more radial and circular motion without baffles. Also, the LSPs exhibit more radial movement at the top and bottom of the reactor in the presence of baffles.

The impeller setup also affects the motion of the LSPs in the reactor. For the PBRT setup, due to a lack of the downdraft at the bottom of the reactor, the LSPs have a lower axial velocity when compared to the PBPB setup. We can also conclude from the data that although LSPs are free-flowing, they are not entirely flow-following in their behaviour. This can also be derived from their respective Strokes number (St), which is greater than 1.

From the data, it can be concluded that the pressure sensor is highly accurate in determining the axial position of the LSP. The IMU shows a high degree of reliability when determining the velocity of the LSP. If a choice has to be made between the IMU and the pressure sensor for use in a future LSP, the pressure sensor would be a more logical choice as it can determine the position of the LSP during the time of measurement, thus giving semi-Lagrangian measurements. The IMU would be an ideal choice to study the flow characteristics of the LSPs in the reactor as they can provide reliable velocity data. The optimal choice would be an LSP that combines

both the aforementioned sensor types working in synergy to provide accurate spatial and temporal data of the LSP in the reactor.

Thus, the LSPs are successfully designed and constructed from off-the-shelf components, tested in two bioreactor setups, and validated using visual tracking methods. These LSPs are the first generation of LSPs with a long way to go from being a fully integrated part of a bioreactor setup. Nevertheless, they are a right step in that direction. There are still some major and minor issues that can be worked upon by future generations of the LSPs.

In terms of future work, the LSPs can be made with multiple sensor units integrated into a single chip. These sensors may include but not be limited to pressure sensors, IMU and temperature sensors, which are readily available on the market and can be integrated with little effort. Some advanced sensors that can also be integrated are pH sensors, dissolved oxygen sensors etc.

Further studies can be conducted with a better experimental setup with multiple cameras at varied heights, focused on different sections of the reactor and then include the 3D tracking using the mirror reflection for more comprehensive data on motion inside the reactor. Also, the tracking code can be improved to monitor and track each LSP individually by differentiating them based on the colour of the LEDs used in them. Combined with the 3D Image of the reactor, this will provide invaluable data and the exact spacial temporal position of each LSP in the reactor and its derivative data and allow for the tracking of the LSP throughout the duration of motion.

The sensors and the internal circuitry can be prefabricated with exact specifications to allow for precise control over the density of the LSP, which will further reduce the errors in the experiment. The shell design can also be improved to allow for rapid assembly and disassembly of the LSPs and prevent any leakage into the shell resulting in damaged circuitry and change in density.

The prospect of getting the positional coordinates from the IMU sensor is not usable due to the dead reckoning and critical drift errors. Two methods can improve this, first is to add a second more reliable but limited positional sensor like a pressure sensor or GPS sensor to

the unit to work with the IMU data and reduce its errors using a unified sensor approach. The second method is to develop a more suitable working code for data processing based on the Kalman Filters in addition to an AHRS algorithm for more promising positional tracking.

The pressure sensors of higher measuring frequency and higher fidelity can be used to get additionally refined data with fewer errors on the axial position of the LSPs. Also, wireless transmission of the data can be used for smaller reactors to get real-time data from the sensors in addition to or in place of recorded data from the SD card. All these components require a larger capacity processor, as the ATTiny 85 microprocessor used in this project may have been sufficient for one sensor. Still, it does not have enough space for multiple sensor units with more complex functionalities.

Thus by continual development and testing of the LSPs in a simulated reactor setting, the goal of developing a fully functional multi-sensor LSP can be achieved. These sensors would be free-flowing and have full positional tracking inside a bioreactor. They could provide excellent data on the study of the rapid changes occurring inside a bioreactor. This data can be further integrated with the reactor's control system for precise control of a bioreactor, thus creating a truly SMART bioreactor.

Bibliography

[Ada19] *Adafruit LPS33HW Water Resistant Pressure Sensor - STEMMA QT : ID 4414 : $12.50 : Adafruit Industries, Unique & fun DIY electronics and kits.* `https://www.adafruit.com/product/4414`, 2019. (Accessed on 04/27/2023).

[Agg14] Aggarwal, S. *What's fueling the biotech engine—2012 to 2013. Nature biotechnology*, 32(1):32–39, 2014.

[Ahm13] Ahmad, N., Ghazilla, R.A.R., Khairi, N.M. and Kasi, V. *Reviews on various inertial measurement unit (IMU) sensor applications. International Journal of Signal Processing Systems*, 1(2):256–262, 2013.

[Ahm22] Ahmad, A., Banat, F., Alsafar, H. and Hasan, S.W. *Algae biotechnology for industrial wastewater treatment, bioenergy production, and high-value bioproducts. Science of The Total Environment*, 806:150585, 2022. ISSN 0048-9697. doi:https://doi.org/10.1016/j.scitotenv.2021.150585.

[Ama04] Amanullah, A., Buckland, B.C. and Nienow, A.W. *Mixing in the fermentation and cell culture industries. Handbook of industrial mixing: science and practice*, pp. 1071–1170, 2004.

[Bar12] Barradas, O., Jandt, U., Da Minh Phan, L., Villanueva, M.E., Schaletzky, M., Rath, A., Freund, S., Reichl, U., Skerhutt, E., Scholz, S., Noll, T., Sandig, V., Pörtner, R. and Zeng, A.P. *Evaluation of criteria for bioreactor*

comparison and operation standardization for mammalian cell culture. Engineering in Life Sciences, 12(5):518–528, 2012. ISSN 16180240. doi:10.1002/elsc.201100163.

[Bis20] Bisgaard, J., Muldbak, M., Cornelissen, S., Tajsoleiman, T., Huusom, J.K., Rasmussen, T. and Gernaey, K.V. *Flow-following sensor devices: A tool for bridging data and model predictions in large-scale fermentations. Computational and structural biotechnology journal*, 18:2908–2919, 2020. ISSN 2001-0370. doi:10.1016/j.csbj.2020.10.004.

[Bis21] Bisgaard, J., Muldbak, M., Tajsoleiman, T., Rydal, T., Rasmussen, T., Huusom, J.K. and Gernaey, K.V. *Characterization of mixing performance in bioreactors using flow-following sensor devices. Chemical Engineering Research and Design*, 174:471–485, 2021. ISSN 0263-8762. doi:https://doi.org/10.1016/j.cherd.2021.08.008.

[BNO17] *BNO055 for Arduino - BlueDot.* `https://www.bluedot.space/products/bno055/`, 2017. (Accessed on 04/27/2023).

[Bos14] Bosch. *Data sheet BNO055 Intelligent 9-axis absolute orientation sensor*, 2014.

[Bru17] Brunner, M., Braun, P., Doppler, P., Posch, C., Behrens, D., Herwig, C. and Fricke, J. *The impact of pH inhomogeneities on CHO cell physiology and fed-batch process performance - two-compartment scale-down modelling and intracellular pH excursion. Biotechnology journal*, 12(7), 2017. doi:10.1002/biot.201600633.

[Bun19] Buntkiel, L., Reinecke, S.F. and Hampel, U. *3.5 - Inertiale Lage- und Bewegungsverfolgung für instrumentierte Strömungsfolger zur Strömungscharakterisierung.* In *Tagungsband*, pp. 52–58. AMA Service GmbH, Von-Münchhausen-Str. 49, 31515 Wunstorf, Germany, 2019. doi:10.5162/14dss2019/3.5.

[Bun20] Buntkiel, L., Reinecke, S. and Hampel, U. *E6. 1 Towards 3D-Motion Tracking of Instrumented Flow Follow-ers in Large Vessels. SMSI 2020-Measurement Science*, pp. 309–310, 2020.

[Cab21] Cabrera, F. and Cobelli, P.J. *Design, construction and validation of an instrumented particle for the Lagrangian characterization of flows. Experiments in Fluids*, 62(1), 2021. ISSN 0723-4864. doi:10.1007/s00348-020-03121-3.

[Che16] Chen, K.Y., Patel, S.N. and Keller, S. *Finexus: Tracking precise motions of multiple fingertips using magnetic sensing.* In *Proceedings of the 2016 CHI Conference on Human Factors in Computing Systems*, pp. 1504–1514. 2016.

[Chi09] Chisti, Y. *Shear Sensitivity.* In M.C. Flickinger, editor, *Encyclopedia of Industrial Biotechnology.* John Wiley & Sons, Inc, Hoboken, NJ, USA, 2009. ISBN 9780471799306. doi:10.1002/9780470054581.eib543.

[Cho07] Cho, H.S., Park, S.Y., Ryu, C.M., Kim, J.F., Kim, J.G. and Park, S.H. *Interference of quorum sensing and virulence of the rice pathogen Burkholderia glumae by an engineered endophytic bacterium. FEMS microbiology ecology*, 60(1):14–23, 2007.

[Cho19] Chopra, H. *Programming Of Remote Surveillance Robot And Odometry Sensor Calibration Protocol For CMR's.* Ph.D. thesis, 2019. doi:10.13140/RG.2.2.19813.73446.

[Dia15] Diaz, E.M., de Ponte Müller, F., Jiménez, A.R. and Zampella, F. *Evaluation of AHRS algorithms for inertial personal localization in industrial environments.* In *2015 IEEE International Conference on Industrial Technology (ICIT)*, pp. 3412–3417. IEEE, 2015.

[Dui19] Duisterwinkel, H.A. *Exploring enclosed environments with floating sensors: Mapping using ultrasound.* 2019.

[Eri09] Erickson, L.E. *Bioreactors.* In *Encyclopedia of Microbiology*, pp. 206–211. Elsevier, 2009. ISBN 9780123739445. doi: 10.1016/B978-012373944-5.00136-X.

[Fit21] Fitschen, J., Hofmann, S., Wutz, J., Kameke, A., Hoffmann, M., Wucherpfennig, T. and Schlüter, M. *Novel evaluation method to determine the local mixing time distribution in stirred tank reactors. Chemical Engineering Science: X*, 10:100098, 2021. ISSN 2590-1400. doi:https://doi.org/10.1016/j.cesx.2021.100098.

[Gau23] Gaugler, L., Mast, Y., Fitschen, J., Hofmann, S., Schlüter, M. and Takors, R. *Scaling-down biopharmaceutical production processes via a single multi-compartment bioreactor (SMCB). Engineering in life sciences*, 23(1):e2100161, 2023.

[Gol11] Goldman, R. *Understanding quaternions. Graphical Models*, 73(2):21–49, 2011. ISSN 1524-0703. doi:https://doi.org/10.1016/j.gmod.2010.10.004.

[Guy16] Guy, O.J. and Walker, K.A.D. *Chapter 4 - Graphene Functionalization for Biosensor Applications.* In S.E. Saddow, editor, *Silicon Carbide Biotechnology (Second Edition)*, pp. 85–141. Elsevier, second edition edn., 2016. ISBN 978-0-12-802993-0. doi:https://doi.org/10.1016/B978-0-12-802993-0.00004-6.

[Hac09] Hacker, D.L., De Jesus, M. and Wurm, F.M. *25 years of recombinant proteins from reactor-grown cells — Where do we go from here? Biotechnology Advances*, 27(6):1023–1027, 2009. ISSN 0734-9750. doi:https://doi.org/10.1016/j.biotechadv.2009.05.008. Biotechnology for the Sustainability of Human Society.

[Hof88] Hofmeester, J.J. *Gas hold-up measurements in bioreactors. Trends in Biotechnology*, 6(1):19–22, 1988. ISSN 0167-7799. doi:https://doi.org/10.1016/0167-7799(88)90109-6.

[Hof22] Hofmann, S., Weiland, C., Fitschen, J., von Kameke, A., Hoffmann, M. and Schlüter, M. *Lagrangian sensors in a stirred tank reactor: Comparing trajectories from 4D-Particle Tracking Velocimetry and Lattice-Boltzmann simulations. Chemical Engineering Journal*, 449:137549, 2022. ISSN 1385-8947. doi:https://doi.org/10.1016/j.cej.2022.137549.

[Jad13] Jadhav, V., Hackl, M., Druz, A., Shridhar, S., Chung, C.Y., Heffner, K.M., Kreil, D.P., Betenbaugh, M., Shiloach, J., Barron, N. *et al.*. *CHO microRNA engineering is growing up: recent successes and future challenges. Biotechnology advances*, 31(8):1501–1513, 2013.

[Jun18] Junne, S. and Neubauer, P. *How scalable and suitable are single-use bioreactors? Current Opinion in Biotechnology*, 53:240–247, 2018. ISSN 0958-1669. doi:https://doi.org/10.1016/j.copbio.2018.04.003. Chemical Biotechnology • Pharmaceutical Biotechnology.

[Kam22] Kamp, M. *Experimental investigation of the flow behavior of Lagrangian LED Particles in a 200 l bioreactor*. Ph.D. thesis, Technische Universität Hamburg, 2022.

[Kla17] Klančar, G., Zdešar, A., Blažič, S. and Škrjanc, I. *Chapter 5 - Sensors Used in Mobile Systems*. In G. Klančar, A. Zdešar, S. Blažič and I. Škrjanc, editors, *Wheeled Mobile Robotics*, pp. 207–288. Butterworth-Heinemann, 2017. ISBN 978-0-12-804204-5. doi:https://doi.org/10.1016/B978-0-12-804204-5.00005-6.

[Kov13] Kovvali, N., Banavar, M. and Spanias, A. *An introduction to kalman filtering with matlab examples. Synthesis Lectures on Signal Processing*, 6(2):1–81, 2013.

[Kra03] Kraft, E. *A quaternion-based unscented Kalman filter for orientation tracking*. In *Proceedings of the sixth interna-*

tional conference of information fusion, vol. 1, pp. 47–54. IEEE Cairns, 2003.

[Kum07] Kumar, N., Gammell, P. and Clynes, M. *Proliferation control strategies to improve productivity and survival during CHO based production culture: a summary of recent methods employed and the effects of proliferation control in product secreting CHO cell lines. Cytotechnology*, 53:33–46, 2007.

[Kun16] Kunert, R. and Reinhart, D. *Advances in recombinant antibody manufacturing. Applied microbiology and biotechnology*, 100:3451–3461, 2016.

[Kus20] Kuschel, M. and Takors, R. *Simulated oxygen and glucose gradients as a prerequisite for predicting industrial scale performance a priori. Biotechnology and bioengineering*, 117(9):2760–2770, 2020. doi:10.1002/bit.27457.

[Lap04] Lapin, A., Müller, D. and Reuss, M. *Dynamic Behavior of Microbial Populations in Stirred Bioreactors Simulated with EulerLagrange Methods: Traveling along the Lifelines of Single Cells. Industrial & Engineering Chemistry Research*, 43(16):4647–4656, 2004. doi:10.1021/ie030786k.

[Lar06] Lara, A.R., Galindo, E., Ramírez, O.T. and Palomares, L.A. *Living With Heterogeneities in Bioreactors: Understanding the Effects of Environmental Gradients on Cells. Molecular Biotechnology*, 34(3):355–382, 2006. doi:10.1385/MB:34:3:355.

[Lau17] Lauterbach, T., Lenk, F., Walther, T., Grösel, M., Lenk, S., Gernandt, T., Moll, R., Seidel, F., Brunner, D., Lüke, T., Hedayat, C., Büker, M.J. and Peters, A. *2.6 -Sens-o-Spheres – Mobile, miniaturisierte Sensorplattform für die ortsungebundene Prozessmessung in Reaktionsgefäßen.*

In *Tagungsband*, pp. 89–93. AMA Service GmbH, Von-Münchhausen-Str. 49, 31515 Wunstorf, Germany, 2017. doi:10.5162/13dss2017/2.6.

[Lau19a] Lauterbach, T., Lüke, T., Büker, M.J., Hedayat, C., Gernandt, T., Moll, R., Grösel, M., Lenk, S., Seidel, F., Brunner, D., Bley, T., Walther, T. and Lenk, F. *Measurements on the fly– Introducing mobile micro-sensors for biotechnological applications. Sensors and Actuators A: Physical*, 287:29–38, 2019. ISSN 09244247. doi: 10.1016/j.sna.2019.01.003.

[Lau19b] Lauterbach, T., Ziebart, N., Bley, T., Walther, T. and Lenk, F. *Mobile Sensoren für die Biotechnologie – Ortsunabhängige, miniaturisierte Prozessmessung. Chemie Ingenieur Technik*, 91(12):1827–1832, 2019. ISSN 0009-286X. doi:10.1002/cite.201900114.

[Li10] Li, F., Vijayasankaran, N., Shen, A., Kiss, R. and Amanullah, A. *Cell culture processes for monoclonal antibody production.* In *MAbs*, vol. 2, pp. 466–479. Taylor & Francis, 2010.

[Mac22] MacDonald, M.A., Nöbel, M., Martínez, V.S., Baker, K., Shave, E., Gray, P.P., Mahler, S., Munro, T., Nielsen, L.K. and Marcellin, E. *Engineering death resistance in CHO cells for improved perfusion culture.* In *Mabs*, vol. 14, p. 2083465. Taylor & Francis, 2022.

[Mad10] Madgwick, S. *et al.. An efficient orientation filter for inertial and inertial/magnetic sensor arrays. Report x-io and University of Bristol (UK)*, 25:113–118, 2010.

[Mah08] Mahony, R., Hamel, T. and Pflimlin, J.M. *Nonlinear complementary filters on the special orthogonal group. IEEE Transactions on automatic control*, 53(5):1203–1218, 2008.

[Mar04] Martin, I., Wendt, D. and Heberer, M. *The role of bioreactors in tissue engineering. Trends in biotechnology*, 22(2):80–86, 2004. ISSN 0167-7799. doi:10.1016/j.tibtech.2003.12.001.

[Mar05] Martin, Y. and Vermette, P. *Bioreactors for tissue mass culture: design, characterization, and recent advances. Biomaterials*, 26(35):7481–7503, 2005. ISSN 0142-9612. doi:10.1016/j.biomaterials.2005.05.057.

[Meh12] Mehmood, N. and Aziz, S.M. *Magnetic sensing technology for in vivo tracking.* In *2012 International Conference on Emerging Technologies*, pp. 1–4. IEEE, 2012.

[Mid79] Middleton, J.C. *Measurment of circulation within large mixing vessels. Third European conference on MIXING*, 1979.

[Moo11] MooYoung, M. *Comprehensive Biotechnology (Second Edition).* Elsevier Science, 2011. ISBN 978-0-08-088504-9.

[Mro16] Mross, S., Zimmermann, T., Winkin, N., Kraft, M. and Vogt, H. *Integrated multi-sensor system for parallel in-situ monitoring of cell nutrients, metabolites, cell density and pH in biotechnological processes. Sensors and Actuators B: Chemical*, 236:937–946, 2016.

[Ope09] *OpenLog Hookup Guide - SparkFun Learn.* `https://learn.sparkfun.com/tutorials/openlog-hookup-guide?_ga=2.110941574.267612023.1687859862-1537849134.1687859862#resources-and-going-further`, 2009. (Accessed on 04/27/2023).

[Oue06] Ouellette, N.T., Xu, H. and Bodenschatz, E. *A quantitative study of three-dimensional Lagrangian particle tracking algorithms. Experiments in Fluids*, 40:301–313, 2006.

[Pat06] Patil, A., Kim, D. and Ni, L. *A study of frequency interference and indoor location sensing with 802.11b and Bluetooth technologies. IJMC*, 4:621–644, 2006. doi: 10.1504/IJMC.2006.010359.

[Pau20] Paul, K. and Herwig, C. *Scale-down simulators for mammalian cell culture as tools to access the impact of inhomogeneities occurring in large-scale bioreactors. Engineering in life sciences*, 20(5-6):197–204, 2020. ISSN 1618-0240. doi:10.1002/elsc.201900162.

[Rei12] Reinecke, S., Deutschmann, A., Jobst, K., Kryk, H., Friedrich, E. and Hampel, U. *Flow following sensor particles—Validation and macro-mixing analysis in a stirred fermentation vessel with a highly viscous substrate. Biochemical Engineering Journal*, 69:159–171, 2012. ISSN 1369703X. doi:10.1016/j.bej.2012.09.010.

[Rei15] Reinecke, S. and Hampel, U. *P8.2 - Instrumentierte Strömungsfolger mit erweiterter Positionsdetektion und Auftriebseinheit.* In *Tagungsband*, pp. 291–296. AMA Service GmbH, Von-Münchhausen-Str. 49, 31515 Wunstorf, Germany, 2015. doi:10.5162/12dss2015/P8.2.

[Rei16] Reinecke, S.F. and Hampel, U. *Instrumented flow-following sensor particles with magnetic position detection and buoyancy control. Journal of Sensors and Sensor Systems*, 5(1):213–220, 2016. doi:10.5194/jsss-5-213-2016.

[Rei17] Reinecke, S.F., Deutschmann, A., Jobst, K. and Hampel, U. *Macro-mixing characterisation of a stirred model fermenter of non-Newtonian liquid by flow following sensor particles and ERT. Chemical Engineering Research and Design*, 118:1–11, 2017. ISSN 02638762. doi:10.1016/j.cherd.2016.12.002.

[Ros18] Rosseburg, A., Fitschen, J., Wutz, J., Wucherpfennig, T. and Schlüter, M. *Hydrodynamic inhomogeneities in large scale stirred tanks – Influence on mixing time. Chemical Engineering Science*, 188:208–220, 2018. ISSN 00092509. doi:10.1016/j.ces.2018.05.008.

[Shr06] Shrout, J.D., Chopp, D.L., Just, C.L., Hentzer, M., Givskov, M. and Parsek, M.R. *The impact of quorum sensing and swarming motility on Pseudomonas aeruginosa biofilm formation is nutritionally conditional. Molecular microbiology*, 62(5):1264–1277, 2006.

[Sie11] Sieblist, C., Jenzsch, M., Pohlscheidt, M. and Lübbert, A. *Insights into large-scale cell-culture reactors: I. Liquid mixing and oxygen supply. Biotechnology journal*, 6(12):1532–1546, 2011. doi:10.1002/biot.201000408.

[Sma22] Smakman, F. and Hall, A.R. *Exposure to lysed bacteria can promote or inhibit growth of neighboring live bacteria depending on local abiotic conditions. FEMS Microbiology Ecology*, 98(2):fiac011, 2022.

[Ste15] Stewart, R.L., Šutalo, I.D. and Wong, C.Y. *Three-dimensional tracking of sensor capsules mobilised by fluid flow. Measurement Science and Technology*, 26(3):035302, 2015. ISSN 0957-0233. doi:10.1088/0957-0233/26/3/035302.

[Sti19] Stine, J.M. *bPod: A Wireless Integrated Sensor Platform for Continuous Localized Bioprocess Monitoring.* Ph.D. thesis, University of Maryland, College Park, 2019.

[STM17] STMicroelectronics NV. *MEMS pressure sensor: 260-1260 hPa absolute digital output barometer with water-resistant package: Datasheet - Production data*, 2017.

[Tas21] Taskan, A.K. and Alemdar, H. *Obstruction-Aware Signal-Loss-Tolerant Indoor Positioning Using Bluetooth Low*

Energy. Sensors, 21(3), 2021. ISSN 1424-8220. doi: 10.3390/s21030971.

[Thi09] Thiele, S., Schone, S., Voigt, F., Da Silva, M.J. and Hampel, U. *Design of a neutrally buoyant self-powered multi-parameter sensor for data logging in flow applications.* In Sebastian Thiele, Sebastian Schöne, Felix Voigt, Marco Jose Da Silva, and Uwe Hampel, editor, *Design of a Neutrally Buoyant Self-Powered MultiParameter Sensor for Data Logging in Flow Applications*, pp. 1927–1930. IEEE, 2009. ISBN 978-1-4244-4548-6. doi: 10.1109/ICSENS.2009.5398357.

[Thi10] Thiele, S., Da Silva, M.J. and Hampel, U. *Autonomous sensor particle for parameter tracking in large vessels. Measurement Science and Technology*, 21(8):085201, 2010. ISSN 0957-0233. doi:10.1088/0957-0233/21/8/085201.

[Tis10] Tissot, S., Farhat, M., Hacker, D.L., Anderlei, T., Kühner, M., Comninellis, C. and Wurm, F. *Determination of a scale-up factor from mixing time studies in orbitally shaken bioreactors. Biochemical Engineering Journal*, 52(2):181–186, 2010. ISSN 1369-703X. doi:https://doi.org/10.1016/j.bej.2010.08.005.

[Tro07a] Tropea, C., Yarin, A.L. and Foss, J.F. *Springer handbook of experimental fluid mechanics.* Springer, Berlin, 2007. ISBN 9783540251415.

[Tro07b] Tropea, C., Yarin, A.L., Foss, J.F. *et al.. Springer handbook of experimental fluid mechanics*, vol. 1. Springer, 2007.

[Val19] Valk,A.N. *A Comprehensive Study of Bubbly Flow using Sensor Motes.* 2019.

[Viv21] Vivek, V., Eka, F.N. and Chew, W. *Mixing Studies in an Unbaffled Bioreactor using a Computational Model Corroborated with in-situ Raman and Imaging Analyses. Chemical*

Engineering Journal Advances, p. 100232, 2021. ISSN 2666-8211. doi:https://doi.org/10.1016/j.ceja.2021.100232.

[Wan16] Wang, S., Stewart, R.L. and Metcalfe, G. *Visualization of the trapping of inertial particles in a laminar mixing tank. Chemical Engineering Science*, 143:99–104, 2016. ISSN 00092509. doi:10.1016/j.ces.2015.12.023.

[Wat62] Watson, B., Ross, B. and Kay, A. *Telemetering from within the body using a pressure-sensitive radio pill. Gut*, 3:181–186, 1962. ISSN 0017-5749. doi:10.1136/gut.3.2.181.

[Wit19] Wittmann, F., Lambercy, O. and Gassert, R. *Magnetometer-based drift correction during rest in IMU arm motion tracking. Sensors*, 19(6):1312, 2019.

[Zha11] Zhao, H. and Wang, Z. *Motion measurement using inertial sensors, ultrasonic sensors, and magnetometers with extended kalman filter for data fusion. IEEE Sensors Journal*, 12(5):943–953, 2011.

[Zhu04] Zhu, R. and Zhou, Z. *A real-time articulated human motion tracking using tri-axis inertial/magnetic sensors package. IEEE Transactions on Neural systems and rehabilitation engineering*, 12(2):295–302, 2004.

[Zim13a] Zimmermann, R., Fiabane, L., Gasteuil, Y., Volk, R. and Pinton, J.F. *Characterizing flows with an instrumented particle measuring Lagrangian accelerations. New Journal of Physics*, 15(1):015018, 2013. doi:10.1088/1367-2630/15/1/015018.

[Zim13b] Zimmermann, R., Fiabane, L., Gasteuil, Y., Volk, R. and Pinton, J.F. *Measuring Lagrangian accelerations using an instrumented particle. Physica Scripta*, T155:014063, 2013. ISSN 0031-8949. doi:10.1088/0031-8949/2013/T155/014063.

A. BlueDot BNO055 Architecture

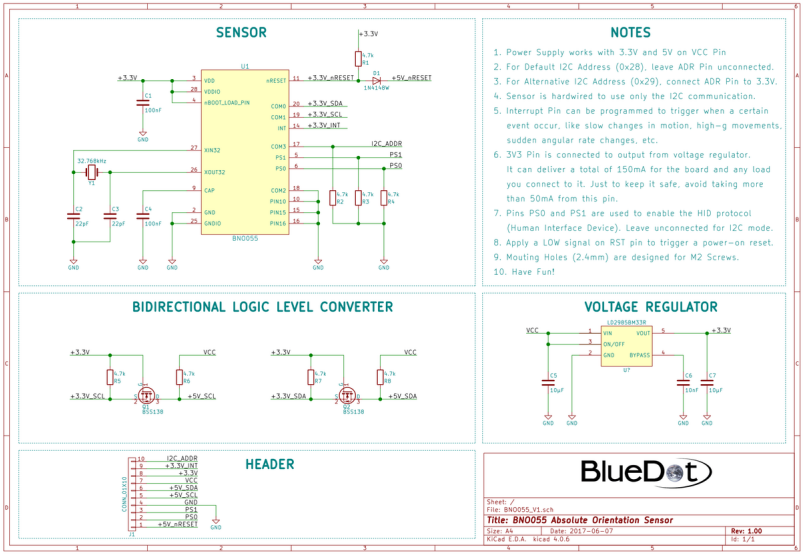

Figure A.1.: The internal architecture of the IMU chip from BlueDot UG, Germany

B. Adafruit LSP33HW Architecture

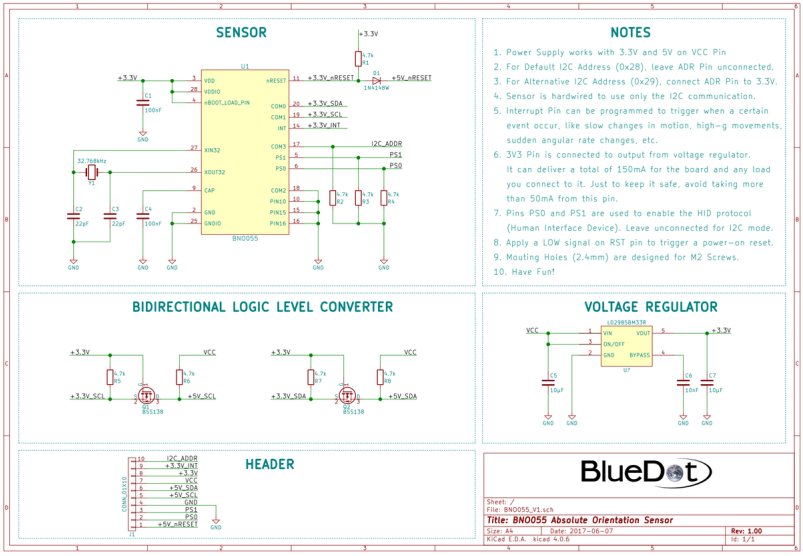

Figure B.1.: The internal architecture of the pressure sensor chip from Adafruit Industries, USA

C. Arduino to ATTiny connection for programming ATTiny

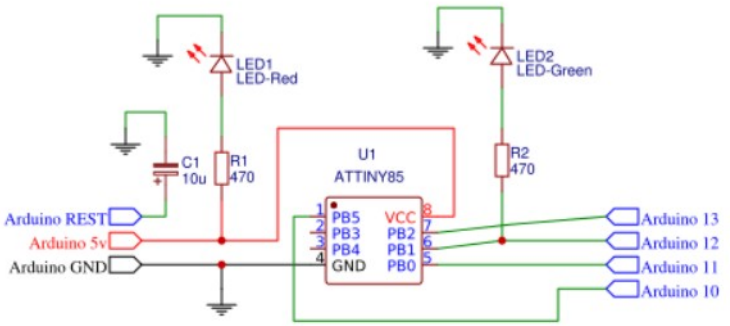

Figure C.1.: Arduino UNO to ATTiny connections for programming the ATTiny.

The Boot-load program for the ATTiny is burnt first on the micro-processor. This is available as a standard with the ATTiny libraries.

D. IMU LSP program

The program for running the IMU LSP can be found in the following GIT repository link.

https://collaborating.tuhh.de/SebastianHofmannIMS/sensor-mote-tracking/-/blob/master/Arduino_Program/IMU_Final/BNO055 _Openlog_New

E. Pressure Sensor LSP Program

The program necessary to operate the IMU LSP can be accessed through the provided GIT repository link.
https://collaborating.tuhh.de/SebastianHofmannIMS/sensor-mote-tracking/-/tree/master/Arduino_Program/Pressure_Final/LPS_ATTiny

F. Pressure LSP post-processing code and data

The code for evaluating the pressure sensor data can be found in the following GitHub repository
https://collaborating.tuhh.de/SebastianHofmannIMS/sensor-mote-tracking/-/tree/master/Matlab/Param_Code_MA/Pressure_Data_Processing/Param_Code_Final

G. IMU LSP post-processing code and data

The code for evaluating the IMU LSP data can be found in the following GitHub repository.
https://collaborating.tuhh.de/SebastianHofmannIMS/sensor-mote-tracking/-/tree/master/Matlab/Param_Code_MA/IMU_Data_Processing/Param_code_final

H. Video Tracking Velocimetry script

The changed VTV script from Kamp can be found in the following GIT repository.
https://collaborating.tuhh.de/SebastianHofmannIMS/sensor-mote-tracking/-/tree/master/Matlab/Param_Code_MA/Image%20processing/Changed%20Maxś%20code

I. Config.txt

The config file for the Openlog used in this study is found in the following GIT repository.

https://collaborating.tuhh.de/SebastianHofmannIMS/sensor-mote-tracking/-/blob/master/Arduino_Program/config.txt

The settings are defined as follows:

Baud: The communication baud rate. The default is 9600bps. Acceptable values that are compatible with the Arduino IDE are 2400, 4800, 9600, 19200, 38400, 57600 and 115200. You can use other baud rates, but you will not be able to communicate with the OpenLog through the Arduino IDE serial monitor.

Escape: The ASCII value (in decimal format) of the escape character. 26 is CTRL+z and is the default. 36 is $ and is a commonly used escape character.

esc#: The number of escape characters required. The default is three, so you must hit the escape character three times to enter command mode. Valid values are from 0 to 254. Setting this to 0 completely disables escape character checking.

Mode: System mode. OpenLog starts in New Log mode (0) by default. Acceptable values are 0=New Log, 1= Sequential Log, 2= Command mode.

verb: Verbose mode. Extended (verbose) error messages are enabled by default. Setting this to 1 will enable verbose error messages (e.g. unknown command: remove !). Setting this to 0 turns off verbose error messages but responds with a ! if there is an error.

Turning off verbose mode is useful when trying to handle errors from an embedded system.

echo: Echo mode. In command mode, characters are echoed by default. Setting this to 0 disables character echo. This is useful if you are debugging and don't want the commands you send to be echoed back to the OpenLog.

ignoreRX: Emergency Reset. Normally OpenLog will perform an emergency reset if the RX pin is pulled low during power up. Setting this to 1 will disable the checking of the RX pin on power up. This can be useful for systems that keep the RX line low for various reasons. If Emergency Override is disabled, you will not be able to force the unit back to 9600bps, and the configuration file will be the only way to change the baud rate.